"Grid Hopping in Sensor Networks: Acceleration Strategies for Single-Step Estimation Algorithms"

Monnoyer de Galland de Carnières, Gilles ; Feuillen, Thomas ; Vandendorpe, Luc ; Jacques, Laurent

ABSTRACT

In radars, sonars, or for sound source localization, sensor networks enable the estimation of parameters that cannot be unambiguously recovered by a single sensor. The estimation algorithms designed for this context are commonly divided into two categories: the two-step methods, separately estimating intermediate parameters in each sensor before combining them; and the single-step methods jointly processing all the received signals. This paper provides a general framework, coined Grid Hopping (GH), unifying existing techniques to accelerate the single-step methods, known to provide robust results with a higher computational time. GH exploits interpolation to approximate evaluations of correlation functions from the coarser grid used in two-step methods onto the finer grid required for single-step methods, hence “hopping” from one grid to the other. The contribution of this paper is two-fold. We first formulate GH, showing its particularization to existing acceleration techniques used in multiple applications. Second, we derive a novel theoretical bound characterizing the performance loss caused by GH in simplified scenarios. We finally provide Monte-Carlo simulations demonstrating how GH preserves the advantages of both the single-step and two-step approaches and compare its performance when used with multiple interpolation techniques.

CITE THIS VERSION

Monnoyer de Galland de Carnières, Gilles ; Feuillen, Thomas ; Vandendorpe, Luc ; Jacques, Laurent. *Grid Hopping in Sensor Networks: Acceleration Strategies for Single-Step Estimation Algorithms.* In: *IEEE Transactions on Signal Processing*, Vol. 72, no.1, p. 4463-4478 (2024) http://hdl.handle.net/2078.1/292969 -- DOI : 10.1109/tsp.2024.3465842

Grid Hopping in Sensor Networks: Acceleration Strategies for Single-Step Estimation Algorithms

Gilles Monnoyer†, Thomas Feuillen, Luc Vandendorpe, Laurent Jacques

***Abstract*—In radars, sonars, or for sound source localization, sensor networks enable the estimation of parameters that cannot be unambiguously recovered by a single sensor. The estimation algorithms designed for this context are commonly divided into two categories: the two-step methods, separately estimating intermediate parameters in each sensor before combining them; and the single-step methods jointly processing all the received signals. This paper provides a general framework, coined Grid Hopping (GH), unifying existing techniques to accelerate the single-step methods, known to provide robust results with a higher computational time. GH exploits interpolation to approximate evaluations of correlation functions from the coarser grid used in two-step methods onto the finer grid required for single-step methods, hence "hopping" from one grid to the other. The contribution of this paper is two-fold. We first formulate GH, showing its particularization to existing acceleration techniques used in multiple applications. Second, we derive a novel theoretical bound characterizing the performance loss caused by GH in simplified scenarios. We finally provide Monte-Carlo simulations demonstrating how GH preserves the advantages of both the single-step and two-step approaches and compare its performance when used with multiple interpolation techniques.**

***Index Terms*—Radar, Localization, Sensor Network, Interpolation, Grid Hopping, Multilateration.**

I. Introduction

SENSOR networks have received growing attention for the last decade in many fields of applications, including remote videoconferencing [1], [2], surveillance [3], autonomous robot [4], [5], automotive or smart-cities applications [6], [7]. In these examples, the sensors composing the networks may be cameras, radars, sonars, microphones, or Ultra-Wide Bandwidth (UWB) receivers. Although those applications use different kinds of sensors with different purposes, they all share a common principle. They leverage the diversity of information gathered by multiple sensors to estimate one or several *parameters of interest*. In this paper, we focus our study on applications in which the network enables the estimation of parameters of interest that cannot be unambiguously recovered by a single sensor. This happens, for example, when a single sensor provides a signal carrying information about distances. Multiple sensors are thereby required to estimate locations as the parameters of interest. In this example, the distances are projections of the location in a reduced space. With the formalism of this paper, we call them the *sensed parameters*. In Fig. 1, we represented this sensing process of one parameter of interest through observations of sensed parameters, with the mathematical formalism we provide in Sec. III.

†Part of this research was supported by the Belgian FNRS

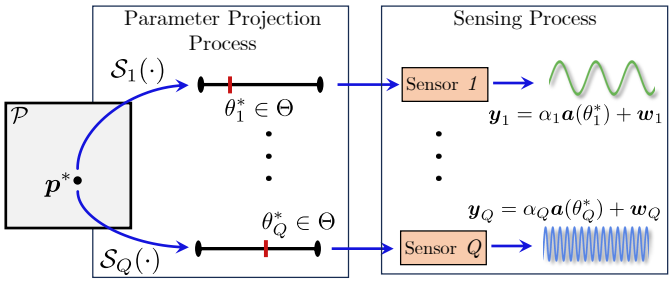

Fig. 1. The two-process acquisition model involved in a sensor network. The q-th sensor ($q \in [Q]$) observes a signal $\boldsymbol{y}_q$ parameterized by the q-th sensed parameter $\boldsymbol{\theta}_q^*$, which is a projection of the parameter of interest $\boldsymbol{p}^*$ from its domain $\mathcal{P}$ onto the sensing domain Θ.

The algorithms used to estimate the parameters of interest can be divided into two main categories. One processes the collected data with *two-step* strategies [8]–[14] and the other with *single-step* approaches [15]–[23]. On the one hand, the two-step methods first perform local processing at each sensor to provide estimates for the sensed parameters. In their second step, they combine these estimates by projecting them onto a space of feasible parameters of interest. This second step is commonly referred to as *multilateration* when the sensed parameters are ranges or delays [14], or *triangulation* when angles are sensed [8]. On the other hand, single-step methods gather all received signals and process them jointly to directly provide estimates for the parameters of interest. This is achieved by maximizing a decision function evaluated in a set, or a grid, of candidate values for the parameters of interest.

Regardless of the network's properties, the main advantage of the two-step strategy resides in its simplicity and its low complexity because the sensed parameters are usually taken from a lower-dimensional domain compared to the domain of interest. However, it is more sensitive to non-idealities such as noise, reverberation, wave occlusion, or interference. The single-step approaches are usually more robust to the above limitations but are computationally heavier [19], [24], [25]. Moreover, estimating multiple parameters of interest with a two-step method requires solving the challenging "data association problem" [26]–[28]. In short, the sensed parameters provided by each sensor need to be correctly associated with one another for the second step. This problem has been addressed in [29] using feature vectors based on the structure of speech signals, or in [30], [31] by means of tracking. Nonetheless, its absence in the single-step procedures makes them more reliable at the price of their higher computational

cost, which we aim to reduce in this paper.

The first contribution of this paper is the presentation of a framework, named Grid Hopping (GH), for the acceleration of the single-step methods. Our framework encapsulates and extends existing acceleration approaches from the literature related to different applicative fields, including Source Localization (SL) of sound or UWB, and multistatic radar. Practically, GH relies on interpolation strategies from one grid, the discretized domain of the sensed parameter, to another grid discretizing the domain of the parameters of interest. A comparison of different interpolation schemes used with the GH framework is performed through extensive Monte-Carlo simulations of several applications in Sec. VIII.

As a second contribution, we provide a novel theoretical bound to quantify the performance of GH. Our bound characterizes the impacts of (i) the nature of the projection of the parameter of interest into the sensed domain (*e.g.*, from a position to a collection of distances), commonly connected to the locations of the sensors, (ii) the density of the grid of parameters of interest, and (iii) the precision loss due to the interpolation strategy used by GH.

The remainder of this paper is structured as follows. Sec. II provides an overview of existing acceleration techniques for single-step methods in different fields of applications. In Sec. III, we derive the global model of signals for a network of sensors collectively observing a parameter of interest. Sec. IV summarizes the conventional implementations of the two-step and the single-step methods. In Sec. V we instantiate the general framework from Sec. III to applications for which the methods from Sec. IV apply. Next, Sec. VI presents our GH formalism and considers its construction using multiple existing interpolation strategies. In Sec. VII, we derive an error bound on the parameter estimation with GH. Sec. VIII presents several simulation results comparing multiple interpolation schemes with the conventional single-step and two-step algorithms. We also compare the actual performance of a single-step algorithm improved with GH with the bound.

Notations: In this paper, $\mathrm{j} = \sqrt{-1}$, lower case bold symbols denote vectors and upper case bold symbols denote matrices. The transpose of a matrix $\boldsymbol{A}$ is $\boldsymbol{A}^\top$, and its More-Penrose inverse is $\boldsymbol{A}^\dagger$. Its largest and the lowest eigenvalues are $\lambda_{\max}(\boldsymbol{A})$ and $\lambda_{\min}(\boldsymbol{A})$. The operator $\delta_{i,j} = 1$ if $i = j$ and 0 otherwise. We refer to the ground truth and the estimate of a quantity a as a^* and $\hat{a}$, respectively. Given $p \in \mathbb{N}$, we use $\mathbb{B}_p(r) := \{\boldsymbol{z} \in \mathbb{R}^d : \|\boldsymbol{z}\|_p \leq r\}$ to denote the ℓ_p-norm ball with radius r. For $N \in \mathbb{N}$, $[N]$ is the index set $\{1, \ldots, N\}$. The scalar product of vectors $\boldsymbol{a}$ and $\boldsymbol{b}$ is denoted by $\langle \boldsymbol{a}, \boldsymbol{b} \rangle$.

II. Related Work

The single-step methods have been studied independently in different signal sensing communities, each proposing specific acceleration strategies.

In the multistatic radar field, a single-step method, often referred to as *joint* [15], [16] or *direct* [18]–[20], has arisen in connection with the sparse signal recovery literature as an application of the Block Orthogonal Matching Pursuit (BOMP) algorithm proposed by Y. C. Eldar in [32]. In those applications, the collection of targets' parameters is represented as a sparse vector in the location-velocity space. Yet, the discretization of the 4D (or 6D) location-velocity space is a limitation that makes such single-step method unsuitable for real-time applications. Acceleration techniques have been suggested in [17], [33] to factorize the model, enabling the sequential estimation of locations and velocities with reduced computation time. Real-time single-step estimation nonetheless remains challenging in multistatic radar applications.

In the SL community, the Steered Response Power (SRP) algorithm is an instance of a single-step method [34], [35]. Many low-complexity strategies have been proposed to decrease the computational complexity of SRP. In [34], the authors propose different techniques to restrict the research to a subset of the domain of interest. In [36], a hybrid approach between the single-step and two-step paradigms is developed by leveraging the intrinsic properties of speech signals to first perform a two-step estimation and then correct it with a single-step-like approach to avoid data-association issues. Other techniques, such as the stochastic region contraction proposed in [37] or grid rescaling methods from [23], [38], [39], propose to iteratively refine the search space, starting from a coarse search of candidates. In [21], [22], the authors propose a volumetric technique that enables the representation of multiple grid bins into a single one, enabling the search on a coarser grid. In the contributions above, the SRP map is computed from the computation of the Generalized Cross-Correlation (GCC) [40]. As shown in Sec. VI, this mapping is an approximation that can be assimilated as the most simple particularization of GH.

In [41], the authors propose a low-complexity single-step algorithm exploiting the sampling properties of the speech signals to build an interpolation-based mapping from the delay grid bins to the location grid. GH generalizes this work for other applications as well as other interpolation schemes.

Recently, we proposed an experimental validation of a specific case of application GH to the Multistatic Radar (MSR) context [42], hence accelerating existing single-step methods in that context. This paper provides the generalization and complementary theoretical validation of this work. The bound derived in Sec. VII enables us to quantify the performance loss caused by the use of GH with different interpolation schemes, including the one presented in [41] and the polar interpolation [43] which is popular for continuous sparse signal processing [44], [45].

III. Problem Statement: The Multi-sensor Model

We consider the general problem of estimating a *parameter of interest* denoted by $\boldsymbol{p}^*$ from the signals received by Q distinct sensors. We focus on systems in which each sensor is only sensitive to a certain projection of $\boldsymbol{p}^*$ onto a low-dimensional observation space, from which $\boldsymbol{p}^*$ may not be retrieved unambiguously. Our generalized model for such sensor networks interprets the measurement as a composition of two processes: *(i)* the parameter projection process, which projects the parameter of interest into the sensing space, and *(ii)* the sensing process that provides the received signals as functions of the sensed parameters (see Fig. 1).

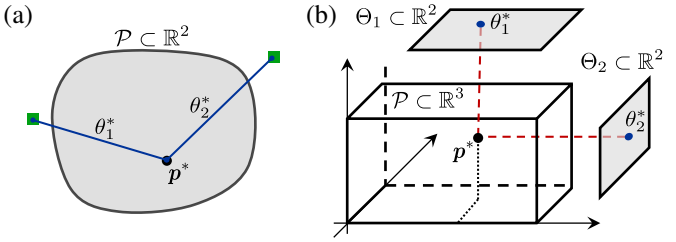

Fig. 2. Two examples of PPFs, *i.e.*, $\mathcal{S}(\cdot)$, where the parameter of interest $\boldsymbol{p}^*$ is a location. **(a)** The sensed parameters are distances between $\boldsymbol{p}$ and reference locations. **(b)** The sensed parameter is a 2D location in a plane corresponding to an image projection of the 3D domain of interest.

In our model of a Q-node sensor network, the q-th sensor ($q \in [Q]$) only observes a projection of the parameter of interest $\boldsymbol{p}^*$, belonging to some space $\mathcal{P} \subset \mathbb{R}^d$, onto a reduced sensing domain $\Theta \subset \mathbb{R}^{\tilde{d}}$. That sensor thus only has access to the *sensed parameter* θ_q^* through a specific Parameter Projection Function (PPF) $\mathcal{S}_q$,

$$\mathcal{S}_q : \mathcal{P} \to \Theta : \theta_q^* = \mathcal{S}_q(\boldsymbol{p}^*). \tag{1}$$

While $\boldsymbol{p}^*$ has a physical meaning, it is not required that θ_q^* has one. We provide in Fig. 2 simple examples of PPFs where $\boldsymbol{p}^*$ is a location whose projection θ_q^* lies in a reduced domain. Examples of expressions for the PPF are given in table I for some typical applications.

The definition of the PPF comes with crucial assumptions.

Assumption 1 (PPF)**.** *The* global *PPF defined as*

$$\mathcal{S}(\boldsymbol{p}) := \big(\mathcal{S}_1(\boldsymbol{p}), \cdots, \mathcal{S}_Q(\boldsymbol{p})\big)^\top \tag{2}$$

is injective over $\mathcal{P}$. Equivalently, $\mathcal{S}$ is a bijection between $\mathcal{P}$ and the admissible sensing domain

$$\mathcal{T} := \mathcal{S}(\mathcal{P}) := \{\boldsymbol{\theta} = \mathcal{S}(\boldsymbol{p}) : \boldsymbol{p} \in \mathcal{P}\}. \tag{3}$$

The domains $\mathcal{P}$, Θ, and $\mathcal{T}$ are all assumed bounded.

To properly define GH and its associated upper bound, we also assume that, for all $q \in [Q]$, $\mathcal{S}_q$ is differentiable over $\mathcal{P}$. Assumption 1 is necessary for the network to recover $\boldsymbol{p}^*$ unambiguously because the sensing process only enables observing its transformation through the global PPF. Without this assumption, two distinct values of $\boldsymbol{p}^*$ may provide exactly the same set of Q received signals, even in noiseless conditions. Additionally, one notes the absence of injectivity condition on $\mathcal{S}_q$ taken alone, translating the potential ambiguity in the recovery of $\boldsymbol{p}^*$ with one single sensor.

For simplicity, we set the sensing domain Θ identical for all q and $\tilde{d} = 1$ for the remaining of the paper, such that $\Theta \subset \mathbb{R}$. This simplification restricts the model to one-dimensional sensed parameters such as angles and distances. Still, our approach extends beyond this restriction.

The sensing process corresponding to the observation of a single parameter of interest (*e.g.*, a multistatic radar observing a single moving target, or a single source of sound captured by a network of microphones) is characterized, for the q-th sensor, by the acquisition of a signal parametrized by the sensed parameter $\theta_q^* \in \Theta$. This signal $\boldsymbol{y}_q \in \mathbb{C}^M$ reads

$$\boldsymbol{y}_q = \alpha_q \boldsymbol{a}(\theta_q^*) + \boldsymbol{w}_q = \alpha_q \boldsymbol{a}(\mathcal{S}_q(\boldsymbol{p}^*)) + \boldsymbol{w}_q, \tag{4}$$

where the function (or *atom*) $\boldsymbol{a} : \Theta \mapsto \mathbb{C}^M$ connects, for each $q \in [Q]$, the value θ_q^* to a waveform acquired by the sensor, $\alpha_q \in \mathbb{C}$ models an unknown amplitude and phase, and the noise $\boldsymbol{w}_q$ is assumed white and Gaussian. Up to the noise $\boldsymbol{w}_q$, the recorded signal $\boldsymbol{y}_q$ is thus 1-sparse in a *parametric* dictionary $\mathcal{A} := \{\boldsymbol{a}(\theta) : \theta \in \Theta\}$ [46], [47]. The model (4) easily generalizes to the joint estimation of K parameters of interest but we restrict our analysis to $K = 1$.

The model (4) implicitly assumes that the network is composed of homogeneous sensors whose node signals are all representable in the same dictionary $\mathcal{A}$. This means, for example, that the multistatic radar presented in Sec. V-A must be composed of radars operating on identical modulation and acquisition settings. Similarly, the arrays of sub-receivers composing the Direction of Arrival (DoA)-based localization system described in Sec. V-C share an identical spatial geometry of sub-receivers. While our approach extends beyond this restriction, our performance bound is built upon it.

Our approach considers that the atoms of $\mathcal{A}$ respect the following assumptions.

Assumption 2 (Atom function)**.** *The operator $\boldsymbol{a}$ has unit norm $\|\boldsymbol{a}(\theta)\|_2 = 1$ for all $\theta \in \Theta$ and is one-to-one over Θ,* i.e.*, $\boldsymbol{a}(\theta) \neq \boldsymbol{a}(\theta')$ for all $\theta \neq \theta' \in \Theta$.*

Assumptions 1 and 2 together ensure the ability of the network to recover $\boldsymbol{p}^*$ unambiguously. Their combination implies that each value of $\boldsymbol{p}^*$ provides its own and unique set of vectors $\{\boldsymbol{a}(\mathcal{S}_q(\boldsymbol{p}^*))\}_{q=1}^Q$.

The derivation of the bound in Sec. VII additionally requires that $\boldsymbol{a}$ generates a *translation invariant* kernel κ [43], [48], [49], *i.e.*,

$$\langle \boldsymbol{a}(\theta), \boldsymbol{a}(\theta') \rangle = \kappa(\theta - \theta'), \quad \forall \theta, \theta' \in \Theta. \tag{5}$$

IV. Single-step and Two-step Methods

We now briefly describe the single-step and the two-step methods, two conventional classes of techniques used to estimate a parameter of interest $\boldsymbol{p}^*$ from a Q-node sensor network according to the measurement model (4), *i.e.*, from the measurements $\{\boldsymbol{y}_q\}_{q=1}^Q$.

a) The two-step methodology: In this methodology, Q estimates $\hat{\boldsymbol{\theta}} := (\hat{\theta}_1, \cdots, \hat{\theta}_Q)^\top$ are first computed by maximizing, for each node $q \in [Q]$, the correlation,

$$\hat{\theta}_q = \arg\max_{\theta \in \Theta} |C_q(\theta)|^2, \quad C_q(\theta) := \langle \boldsymbol{y}_q, \boldsymbol{a}(\theta) \rangle. \tag{6}$$

Next, the estimate $\hat{\boldsymbol{p}}$ is computed from a non-linear least squares minimization

$$\hat{\boldsymbol{p}} = \arg\min_{\boldsymbol{p}' \in \mathcal{P}} \|\hat{\boldsymbol{\theta}} - \mathcal{S}(\boldsymbol{p}')\|_2. \tag{7}$$

This second step is referred to as *multilateration* for ellipses or hyperbolas intersection [9], [14], and *triangulation* for directions intersection [8].

Since the first step is a non-convex continuous optimization over Θ, (6) is generally approximated by restricting θ to a uniform discretization $\Theta_{\mathrm{G}} \subset \Theta$, resulting in

$$\hat{\theta}_q = \underset{\theta \in \Theta_{\mathrm{G}}}{\arg\max}\, |C_q(\theta)|^2. \tag{8}$$

This first estimate can then be improved by, *e.g.*, starting a gradient descent on the cost $-|C_q(\theta)|^2$ in (6) initialized with $\hat{\theta}_q$ [50]–[52]. Alternatively, one can consider faster interpolation techniques to maximize an approximation of C_q [43], [45], [53].

b) The single-step methodology: In this method we look for a value of $\hat{\boldsymbol{p}} \in \mathcal{P}$ directly maximizing the *non-coherent* sum of all measurement correlations with $\mathcal{S}_q(\boldsymbol{p})$, *i.e.*, all signals are jointly processed in the global optimization

$$\hat{\boldsymbol{p}} = \underset{\boldsymbol{p} \in \mathcal{P}}{\arg\max}\, \textstyle\sum_{q\in[Q]} |C_q(\mathcal{S}_q(\boldsymbol{p}))|^2. \tag{9}$$

If all the measurement noises are independent in (4), and all α_q are i.i.d. and independent from $\boldsymbol{p}$, this step is a maximum likelihood estimator [19], [25], [54]. In this case, (9) is equivalent to minimizing $-\log \mathrm{P}(\{\boldsymbol{y}_q\}_{q=1}^{Q} \,|\, \boldsymbol{p}, \boldsymbol{\alpha}) := \sum_{q\in[Q]} \|\boldsymbol{y}_q - \alpha_q \boldsymbol{a}(\mathcal{S}_q(\boldsymbol{p}))\|_2^2$.

The maximization (9) is also often approximated on a uniform discretization $\mathcal{P}_{\mathrm{G}}$ of $\mathcal{P}$ through

$$\hat{\boldsymbol{p}} = \underset{\boldsymbol{p} \in \mathcal{P}_{\mathrm{G}}}{\arg\max}\, \textstyle\sum_{q\in[Q]} |C_q\big(\mathcal{S}_q(\boldsymbol{p})\big)|^2. \tag{10}$$

Similar to the problem (6), the single-step approach (9) can be solved efficiently in its continuous form with solvers that initiate refinement steps on estimates obtained from a grid-search approach (10). This is particularly exemplified by the Multi-snapshot Newtonalized Orthogonal Matching Pursuit [55]. For the intelligibility of the focus of our paper, *i.e.*, the analysis of the GH framework, we limit its scope to the single-step and two-step methods restricted to their grid search version, respectively using (8) and (10) instead of (6) and (9). Since $\boldsymbol{p}^*$ is assumed to be taken from the continuous domain $\mathcal{P}$ unrestricted to the grid $\mathcal{P}_{\mathrm{G}}$, this aspect induces gridding errors that are taken into account in both the theoretical and numerical study of this paper. We note that the GH technique we present in Sec. VI can be coupled with the off-grid search and refinement techniques mentioned above. We postpone this coupling with advanced algorithms estimating multiple parameters of interest from a continuous domain to future contributions.

c) Differences between the two methodologies: Computationally speaking, two-step methods based on the discretization (8) require $N_\Theta := |\Theta_{\mathrm{G}}|$ evaluations of the correlation C_q, for all $q \in [Q]$. On the other hand, single-step methods based on the discretization (10) require $N_{\mathrm{P}} := |\mathcal{P}_{\mathrm{G}}|$ such evaluations for each index q. Since the domain of interest $\mathcal{P}$ is typically of higher dimensions compared to the sensed domain Θ, it results in $N_{\mathrm{P}} \gg N_\Theta$. This intensifies as a higher precision is targeted by the use of denser grids, which is why two-step methods are known to be faster than their single-step counterparts.

The single-step methods, however, potentially offer a more robust estimation of $\boldsymbol{p}^*$ as they directly gather all available information and promote, via the mappings $\mathcal{S}_q(\boldsymbol{p})$, consistent models across all sensors. This has, for example, been shown for signal transmissions submitted to high noise [19] or is subjected to reverberation [24], [25]. The question we address in this work is thus to preserve the advantages of both approaches in a hybrid strategy: Grid Hopping.

V. Examples of applications

Let us provide a few *standard* examples of applications (also summarized in Table I) for which the model and the two classes of methods described above apply. For each application, we describe the contextual meaning of *(i)* the number Q of acquired signals, *(ii)* the length M of the measurements, *(iii)* the sensed parameters $\{\theta_q^*\}_{q=1}^{Q}$, and *(iv)* the parameter of interest $\boldsymbol{p}^*$. Moreover, we provide the parametric expression of the atom $\boldsymbol{a}(\theta)$ and the expression of the PPF, $\mathcal{S}_q(\boldsymbol{p})$.

A. Multistatic FMCW Radar

A MSRs is composed of multiple RXs and one or multiple transmitters (TXs). For simplicity, we consider a single transmitter in a linear chirp modulation setting and a single antenna in each receiver. The MSR estimates the location and the velocity vectors describing a target. With the appropriate simplifications of the radar signal model [17], a Frequency-Modulated Continuous Wave (FMCW) radar can be seen as the combination of a Doppler radar and a radar emitting a single chirp [56]–[58]. For simplicity, we restrict here the application of (4) to the separate estimation of the location and the velocity.

The number of measurements Q is the number of RXs since we assume here a single TX. The dimension M is the number of samples acquired per RX in one processing time frame.

a) Location estimation with a MSR: The parameter of interest $\boldsymbol{p}^*$ is a target's location. The q-th sensed parameter is the sum of distances from the TX to the target and from the target and the q-th RX. Fig. 3(a) illustrates the geometrical properties of those parameters in the MSR application. Given $\boldsymbol{x}^{\mathrm{TX}}$ and $\boldsymbol{x}_q^{\mathrm{RX}}$ as the TX and the q-th RX's locations respectively, the PPF of the q-th receiver

$$\mathcal{S}_q(\boldsymbol{p}) = \tfrac{B}{\mathsf{c}}(\|\boldsymbol{p} - \boldsymbol{x}^{\mathrm{TX}}\|_2 + \|\boldsymbol{p} - \boldsymbol{x}_q^{\mathrm{RX}}\|_2), \tag{11}$$

where $\frac{B}{\mathsf{c}}$ is inserted for the simplicity of the atom's expression in (12), with B is the radar's bandwidth and c the speed of light. As derived in [59], [60], the atom's expression for a single linear-chirp FMCW radar reads

$$a_m(\theta) = \exp(-\mathrm{j}2\pi\theta\tfrac{m}{M}). \tag{12}$$

b) Velocity estimation with a MSR: The target's velocity is now the parameter $\boldsymbol{p}^*$, and the sensed parameters are the bistatic speeds [15], [16]. Given the unit vectors $\boldsymbol{h}^{\mathrm{TX}}$ and $\boldsymbol{h}_q^{\mathrm{RX}}$ pointing toward the target from the TX and the q-th RX, respectively, the PPF linking the velocity vector contained in $\boldsymbol{p}$ to the q-th bistatic speed reads

$$\mathcal{S}_q(\boldsymbol{p}^*) = \tfrac{Mf_0T_{\mathrm{s}}}{\mathsf{c}}\langle \boldsymbol{h}^{\mathrm{TX}} + \boldsymbol{h}_q^{\mathrm{RX}}, \boldsymbol{p}\rangle, \tag{13}$$

similarly normalized with $\frac{Mf_0T_{\mathrm{s}}}{\mathsf{c}}$, where f_0 is the carrier frequency and T_{s} the sampling period. With this normalization, the atom's expression for the Doppler multistatic radar follows the same expression as (12).

Applications		Q	M	$\boldsymbol{p}^*$	parameter projection $\mathcal{S}_q(\boldsymbol{p}) =$	atom $a_m(\theta) =$
Localization with MSR	Fig. 3(a)	# receiver (RX)s antennas	# samples per chirp	target's location	$\frac{B}{\mathsf{c}}(\|\boldsymbol{p}-\boldsymbol{x}^{\mathrm{TX}}\|_2+\|\boldsymbol{p}-\boldsymbol{x}_q^{\mathrm{RX}}\|_2)$	$\exp(\mathrm{j}2\pi\theta m/M)$
Velocity from MSR	Fig. 3(b)	# RXs antennas	# chirps	target's velocity	$\frac{Mf_0T_\mathrm{s}}{\mathsf{c}}\langle \boldsymbol{h}^{\mathrm{TX}}+\boldsymbol{h}_q^{\mathrm{RX}},\,\boldsymbol{p}\rangle$	$\exp(\mathrm{j}2\pi\theta m/M)$
Source Loc. with TDoA	Fig. 3(c)	# pairs of RXs	# Fourier bins used in GCC	source location	$\frac{1}{\mathsf{c}T_\mathrm{s}}(\|\boldsymbol{p}-\boldsymbol{x}_q\|_2-\|\boldsymbol{p}-\boldsymbol{x}'_q\|_2)$	$\exp(\mathrm{j}2\pi\theta m/M)$
Source Loc. with DoA	Fig. 3(d)	# sensor arrays	# sub-receivers per array	source location	$\angle(\boldsymbol{p}-\boldsymbol{x}_q^{\mathrm{RX}})$	$\exp(\mathrm{j}2\pi\lambda^{-1}\,\boldsymbol{h}_m^\top\boldsymbol{e}_\theta)$

TABLE I
SUMMARY OF THE APPLICATIONS PRESENTED IN SEC. V WITH THE CONTEXTUAL MEANING OF EACH MODEL QUANTITY ("#" MEANS "NUMBER OF").

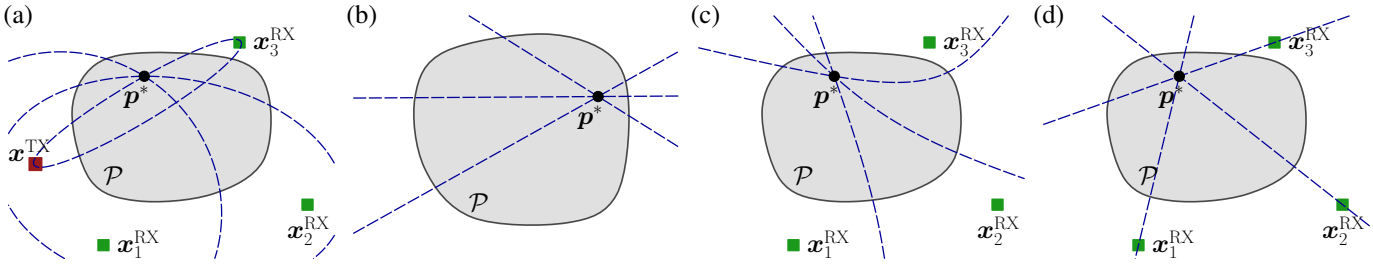

Fig. 3. Representations of the applications described in Sec. V, each with $Q = 3$ measurements. The dashed lines represent the loci of identical sensed parameters in the domain of interest. **(a)** MSR composed of one TX and three RXs, for the estimation of the target location $\boldsymbol{p}^*$. The loci are given by ellipses. **(b)** The same MSR for the estimation of $\boldsymbol{p}^*$ as the target velocity. **(c)** SL system composed of three RX (yielding $Q = 3$ pairs of RXs), with $\boldsymbol{p}$ as the source's location. The loci are hyperbolas. **(d)** SL system composed of three receiving nodes, each composed of an array of L receivers such as depicted in Fig. 4.

B. Source Localization with Time Difference of Arrival

Our approach also applies to the estimation of the location $\boldsymbol{p}^*$ of the source of a signal. When the receivers are not synchronized with the transmitter, the delays cannot be used for intersections of ellipses like in MSR. Therefore, evaluating the Time Difference of Arrival (TDoA) between pairs of receivers is a commonly used strategy that leads to intersections of hyperbolas. A simple representation of this application is shown in Fig. 3(c). This method is typically used in sound source localization [25] or UWB positioning systems [61].

Let L be the number of receivers (such as microphones for sound source localization) located around $\boldsymbol{p}^*$ (see Fig. 3(c)). In our model (4), the number of measurements is $Q = L(L-1)/2$, *i.e.*, to the number of pairs of receivers that we associate to record the TDoA. The measurement $\boldsymbol{y}_q$ from the q-th pair of RXs is obtained at the output of a cross-correlation using a *phase-transform weighting function* [21]. This amounts to computing the Discrete Fourier Transform (DFT) of each of the L received signals, and, given a pair of receivers, multiplying their two spectra and keeping only their phase by modulus division (see *e.g.*, [35] for details).

Mathematically, for a single source, all RXs record the same signal with different unknown delays, leading to

$$a_m(\theta) = \exp(\mathrm{j}2\pi\theta\tfrac{m}{M}), \quad m \in [M], \tag{14}$$

where θ is the TDoA (normalized with respect to the sampling rate T_s for simplicity) so that the PPF is

$$\mathcal{S}_q(\boldsymbol{p}) = \tfrac{1}{\mathsf{c}T_\mathrm{s}}(\|\boldsymbol{p}-\boldsymbol{x}_q\|_2 - \|\boldsymbol{p}-\boldsymbol{x}'_q\|_2), \tag{15}$$

where $\boldsymbol{x}_q$ and $\boldsymbol{x}'_q$ denote the locations of the two receivers of the q-th pair.

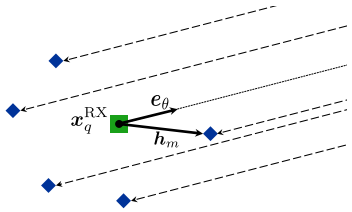

Fig. 4. Representation of the q-th node of a DoA-based application. The node is composed of M co-located sub-receivers such that the source is located in the far field, implying an angle of arrival θ (acting as the sensed parameter) identical for all receivers of a given array.

C. Source localization from Directions of Arrival

Estimating a source location $\boldsymbol{p}^*$ from a collection of Q sensor arrays, each sensitive to a Direction of Arrival (DoA) the wave emitted by the source, also enters into the scope of the model (4). This case typically happens with arrays of microphones [62], [63], or radio frequency receivers [64], and $\boldsymbol{p}^*$ is estimated from the intersection of lines given by the DoAs, such as depicted in Fig. 3(d).

Each sensor array is composed of M sub-receivers as depicted in Fig. 4. The atom function in model (4) corresponds to the *steering vector* which can, for a generic array of receivers, be written following [65], [66],

$$a_m(\theta) = \exp(\mathrm{j}2\pi\lambda^{-1}\,\boldsymbol{h}_m^\top\boldsymbol{e}_\theta), \quad m \in [M], \tag{16}$$

where λ is the signal's wavelength, $\boldsymbol{h}_m$ is the vector pointing from a chosen reference sub-receiver's location toward the m-th sub-receiver, and $\boldsymbol{e}_\theta$ is the unit vector pointing in the direction given by the sensed parameter θ. If the location to estimate $\boldsymbol{p}^*$ lies in 2D, then θ is an angle of arrival defined with respect to an arbitrary reference direction. If, however,

$\boldsymbol{p}^*$ is a 3D position, then θ is a pair of azimuth and elevation angles. In both cases, the PPF reads

$$\mathcal{S}_q(\theta) = \angle(\boldsymbol{p} - \boldsymbol{x}_q^{\mathrm{RX}}). \tag{17}$$

VI. Grid Hopping

The GH methodology is a fast proposition to approximately solve (10). We first intuitively motivate the technique by considering the simple MSR instance of Fig. 5(a), composed of one TX and two RXs. The system acquires a single chirp, taking $M = 10$ samples to determine the location $\boldsymbol{p}^*$ of a single target, thus acquiring a signal modeled according to Sec. V-A a). Fig. 5(b) shows an example of a correlation function used by the single-step method (9) with a typical grid $\mathcal{P}_{\mathrm{G}}$ discretizing the domain of interest $\mathcal{P}$. In Fig. 5(c), we observe the correlations that one maximizes in a two-step approach. The blue samples form a uniform sensing grid Θ_{G} discretizing Θ with a precision similar to the way $\mathcal{P}_{\mathrm{G}}$ discretizes $\mathcal{P}$. The grey samples are taken from the grids $\mathcal{S}_q(\mathcal{P}_{\mathrm{G}})$, which are the transformation of $\mathcal{P}_{\mathrm{G}}$ through the PPFs.

Computationally speaking, the grid search used to *exactly* solve the single-step problem (10) restricted to $\mathcal{P}_{\mathrm{G}}$ requires, for each index $q \in [Q]$, to evaluate the correlation $C_q(\theta)$ for all θ taken from the grid $\mathcal{S}_q(\mathcal{P}_{\mathrm{G}})$. With GH, we use atom interpolation to "hop" from the (blue) grid Θ_{G} onto the (grey) grid $\mathcal{S}_q(\mathcal{P}_{\mathrm{G}})$ for the evaluations of $C_q(\theta)$. This operation is expected to provide a good approximation of the exact single-step grid search with a computational complexity with the same order of magnitude as exhibited by two-step methods, which are commonly faster.

One can understand the performance of GH as follows. Given a ground truth $\boldsymbol{p}^*$, the precision of the estimate $\hat{\boldsymbol{p}}$ resulting from (10) is intrinsically limited by the density of the grid $\mathcal{P}_{\mathrm{G}}$. Yet, as observed in Fig.5(b)-(c), the grids $\mathcal{S}_q(\mathcal{P}_{\mathrm{G}})$ discretize Θ more densely than $\mathcal{P}_{\mathrm{G}}$ discretizes $\mathcal{P}$. Therefore, we expect, and quantify with the bound derived in Sec. VII, that the error caused by interpolating from the lower density grid Θ_{G} toward $\mathcal{S}_q(\mathcal{P}_{\mathrm{G}})$ is often negligible compared to the limitation intrinsically caused by the gridding $\mathcal{P}_{\mathrm{G}}$ of $\mathcal{P}$.

Beyond the intuitive example, we first define the order-I interpolation performed by GH from the partition $\cup_{n\in[N_\Theta]}\Theta_n = \Theta$, with $\Theta_n \cap \Theta'_n = \emptyset$ for $n \neq n'$. With $\{\bar{\theta}_{n,i}\}_{i\in[I]} \subset \Theta_{\mathrm{G}}$ denoting a subset the grid Θ_{G} taken in the neighbourhood of its n-th bin, the interpolated atom $\tilde{\boldsymbol{a}}(\theta)$ approximates $\boldsymbol{a}(\theta)$ as

$$\tilde{\boldsymbol{a}}(\theta) := \sum_{n\in[N_\Theta]} \mathcal{X}_n(\theta) \sum_{i\in[I]} c_{n,i}(\theta)\boldsymbol{a}(\bar{\theta}_{n,i}), \tag{18}$$

where $\mathcal{X}_n(\theta) = 1$ for $\theta \in \Theta_n$ and 0 otherwise, and where the interpolating coefficients are such that $c_{n,i}(\bar{\theta}_{n',i'}) = \delta_{n,i'}\delta_{n,i'}$.

Second, GH uses the interpolated atom (18) in the single-step correlation (10), *i.e.*,

$$\hat{\boldsymbol{p}} = \underset{\boldsymbol{p}\in\mathcal{P}_{\mathrm{G}}}{\arg\max} \sum_{q\in[Q]} |\tilde{C}_q(\mathcal{S}_q(\boldsymbol{p}))|^2, \quad \tilde{C}_q(\theta) := \langle \boldsymbol{y}_q, \tilde{\boldsymbol{a}}(\theta)\rangle. \tag{19}$$

In practice, (19) can be computed efficiently with a lookup table (mapping each $\boldsymbol{p} \in \mathcal{P}_{\mathrm{G}}$ to the right grid index n in Θ_{G}) and by pre-computing the coefficients $\{c_{n,i}(\theta)\}_{i\in[I]}$ for all $\theta \in \mathcal{S}_q(\mathcal{P}_{\mathrm{G}})$ and all $q \in [Q]$. Formally, we have Q pre-computed matrices denoted by $\mathcal{L}_q \in \mathbb{C}^{N_{\mathrm{P}}\times 2I}$. For all $q \in [Q]$, the n_{P}-th row (denoted $\mathcal{L}_q[n_{\mathrm{P}}]$) contains the I indexes to perform the interpolation from the grid Θ_{G}, and the I pre-computed coefficients.

Algorithm 1: Grid-Hopping Single-step Method

Input : The measurement: $\boldsymbol{y}_q$ and the pre-computed lookup tables $\mathcal{L}_q \in \mathbb{C}^{N_{\mathrm{P}}\times 2I}$, for all $q \in [Q]$

Output: The estimate: $\hat{\boldsymbol{p}}$

for $q = 1$ **to** Q **do**

$$\boldsymbol{g}_q = C_q(\Theta_{\mathrm{G}}) \tag{20}$$

for $n_{\mathrm{P}} = 1$ **to** N_{P} **do**

$$(n_1, \ldots, n_I, c_1, \ldots, c_I) \leftarrow \mathcal{L}_q[n_{\mathrm{P}}] \tag{21}$$

$$h_{q,n_{\mathrm{P}}} = \textstyle\sum_{i=1}^{I} c_i\, g_{q,n_i} \tag{22}$$

$$\hat{n}_{\mathrm{P}} = \arg\max_{n_{\mathrm{P}}\in[N_{\mathrm{P}}]} \textstyle\sum_{q=1}^{Q} \left|h_{q,n_{\mathrm{P}}}\right|^2 \tag{23}$$

$$\hat{\boldsymbol{p}} = \hat{n}_{\mathrm{P}}\text{-th element of } \mathcal{P}_{\mathrm{G}} \tag{24}$$

The resulting GH procedure is summarized in Alg. 1. During the real-time processing, we compute, for all $q \in [Q]$, the correlations $C_q(\Theta_{\mathrm{G}})$ in (20). Next, for each $\boldsymbol{p} \in \mathcal{P}_{\mathrm{G}}$, we read the interpolation data in (21) and perform the hopping in (22).

Overall, the QMN_{P} products required for the grid search of the one-step estimation (9) is replaced by the computation of QMN_Θ products for the computation of the Q sets of correlations $C_q(\Theta_{\mathrm{G}})$ plus additional QIN_{P} products for the interpolations (22). Because in non-degenerate conditions $I \ll M$ and $N_\Theta \ll N_{\mathrm{P}}$, the GH-based grid search is expected to be computed faster than the standard single-step computation given in (10).

We end this section by illustrating, in Fig. 6, the approximated correlation functions $\tilde{C}_q(\theta)$ obtained for the simple example presented at the beginning of this section (see Fig. 5) while using the four interpolation schemes that we compare with our numerical results in Sec. VIII: (i) the Zero-Order Hold (ZOH) strategy, *i.e.*, no interpolation, with $I = 1$, (ii) a conventional polynomial interpolation method (Fig. 6(b) for $I = 3$), (iii) the "Polar" interpolation, which is specifically efficient for translation-invariant atoms [43], [44]. Its standard version with $I = 3$ (Fig. 6(c)) has more recently been extended to higher order versions [53]. Finally (iv) the Least-Squares (LS) optimal interpolation, minimizing the interpolation error for a given order I, such that $(c_1, \cdots c_I)^\top = [\boldsymbol{a}(\bar{\theta}_1), \cdots, \boldsymbol{a}(\bar{\theta}_I)]^\dagger \boldsymbol{a}(\theta)$ (Fig. 6(d) for $I = 3$).

VII. Upper Bound on the GH Estimation

This section theoretically studies the estimation errors resulting from the approximations used in our GH strategy. Let

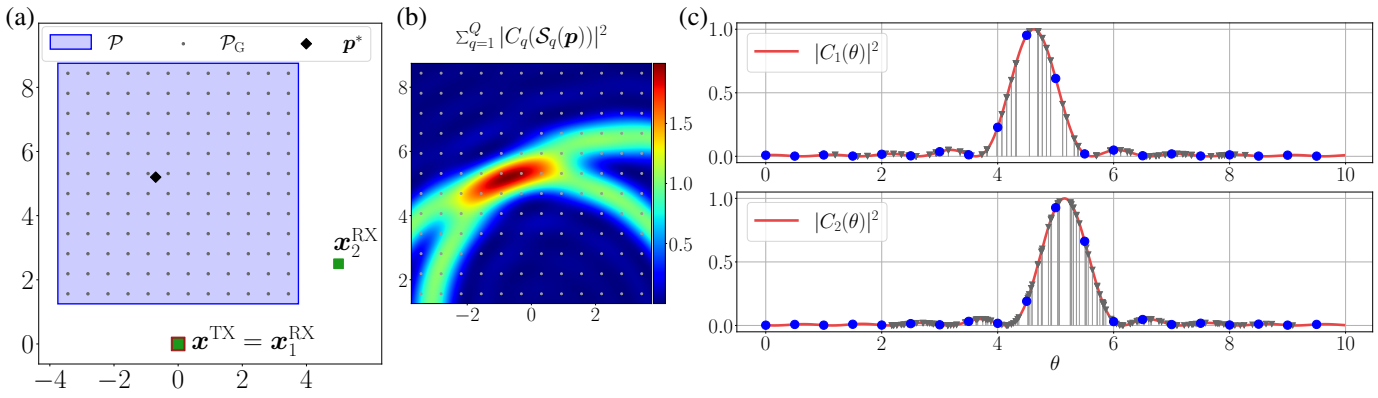

Fig. 5. **(a)** Schematic representation of an example of a MSR composed of one TX and two RXs. The received signals are composed of $M = 10$ samples we have $\frac{B}{c} = 0.5$. The grid of grey dots represents the elements of $\mathcal{P}_\mathrm{G}$. **(b)** The resulting noiseless single-step correlation function used by (9), or evaluated only to the grid $\mathcal{P}_\mathrm{G}$ by (10). **(c)** The correlation function of the first step (6) for $q = 1$ (top) and $q = 2$ (bottom) corresponding to two RXs in the situation described in (a). The big blue dots represent the samples taken on the grid Θ_G. The dense stem plot in grey depicts the samples taken on the grids $\mathcal{S}_q(\mathcal{P}_\mathrm{G})$.

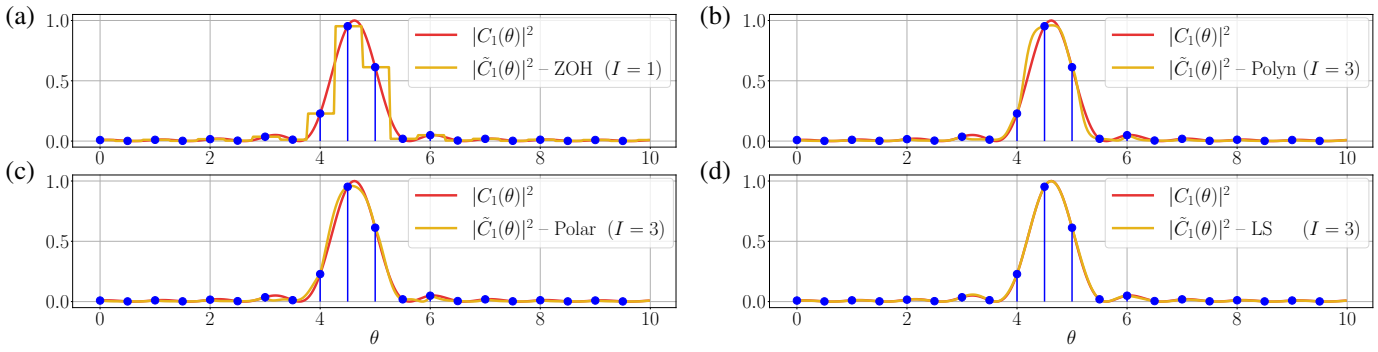

Fig. 6. Comparison of the exact correlation function $C_q(\theta)$ and its approximation $\tilde{C}_q(\theta)$ resulting either from **(a)** the NN strategy (no interpolation), **(b)** an order-2 polynomial interpolation ($I = 3$), **(c)** the conventional polar interpolation [43] ($I = 3$), and **(d)** the LS-optimal interpolation with $I = 3$.

us first motivate the study proposed in this section. Assuming a set of measurement vectors $\boldsymbol{y}_q$ described by the model (4), the GH-based single-step estimation (19) produces an estimate $\hat{\boldsymbol{p}}$ with an error $\|\hat{\boldsymbol{p}} - \boldsymbol{p}^*\|_2$ that originates from three aspects:

- *The noise* $\boldsymbol{w}$, affecting any estimation method, including the continuous single-step optimization (9),
- *the restriction to a grid search on* $\mathcal{P}_\mathrm{G}$, affecting both (10) and (19),
- and *the interpolation error*, specific to our GH approach.

While the stochastic errors caused by the noise are efficiently characterized by the well-known Cramèr-Rao Lower Bound (CRLB) [67]–[69], we evaluate here the estimation errors specifically caused by the two latest, deterministic, effects within the sensor network context of this paper. To that end, we derived an upper bound on the error $\|\hat{\boldsymbol{p}} - \boldsymbol{p}^*\|_2$ for an estimate $\hat{\boldsymbol{p}}$ resulting from (19) while considering *noiseless* measurements. We express our bound with respect to the properties of the grids Θ_G and $\mathcal{P}_\mathrm{G}$ as well as the interpolator used for GH, showing the joint effect of each processing step.

We note that our bound encompasses the study of the lone effect of either the gridding or the interpolation since it can be particularized to corresponding scenarios by appropriately setting limit values of some variables upon which it is expressed. This aspect is detailed later in this section.

In the remainder of this section, we first define variables describing the estimation context. Next, the upper bound is given in Theorem 1, with its proof deferred to the appendix. At the end of this section, we discuss the insights one learns from our bound and its limitations.

A. Technical Definitions

Our upper bound is formulated using four definitions. With Definitions 1 and 2, we extract variables respectively quantifying the grid's density and the interpolation's accuracy that drive the estimation error under study. Additionally, Definitions 3 and 4 identify attributes characterizing the shape of the single-step estimation's objective function.

In detail, Definition 1 relates the spacing of the grid $\mathcal{P}_\mathrm{G}$ using the concept of "covering radius", denoted by ρ. In words, ρ is the distance within which any $\boldsymbol{p} \in \mathcal{P}$ is guaranteed to find a nearby element from the grid $\mathcal{P}_\mathrm{G}$.

Definition 1. *[Covering radius] The grid $\mathcal{P}_\mathrm{G}$ discretizes $\mathcal{P}$ with the covering radius ρ defined by*

$$\rho := \max_{\boldsymbol{p} \in \mathcal{P}} \min_{\boldsymbol{p}' \in \mathcal{P}_\mathrm{G}} \|\boldsymbol{p} - \boldsymbol{p}'\|_2. \tag{25}$$

A high-density grid corresponds to a small value of ρ, which goes towards 0 for an "infinitely dense" grid. We

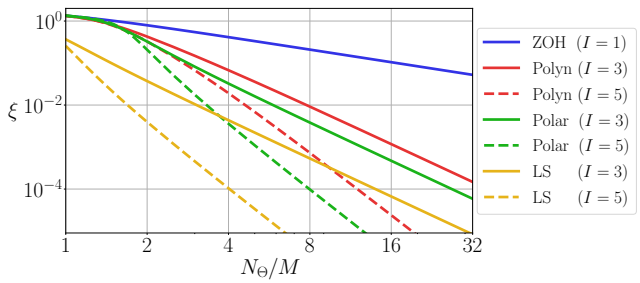

Fig. 7. Interpolation gaps of multiple interpolators applied to the example of Fig. 5: These results are obtained with a sensed grid uniformly discretizing the sensed space $\Theta := [0, M[$ with N_Θ grid bins.

intuitively expect an estimation error that linearly increases with ρ, following the increasing worst-case distance between $\boldsymbol{p}^*$ and its closest neighbor in $\mathcal{P}_\mathrm{G}$.

Next, we evaluate the interpolation accuracy using the *interpolation gap* ξ defined below. As later shown in Theorem 1, the worst-case error also grows linearly with ξ.

Definition 2 (Interpolation Gap)**.** *Given an interpolation scheme from which $\tilde{\boldsymbol{a}}(\theta)$ is derived by* (18)*, we define the* interpolation gap ξ *as*

$$\xi := \max_{\theta\in\Theta} \|\tilde{\boldsymbol{a}}(\theta) - \boldsymbol{a}(\theta)\|_2. \tag{26}$$

Let us highlight that ξ is driven in practice by three elements: (i) the nature of the interpolation, (ii) its order I, and (iii) the density of the grid Θ_G. This dependency is represented in Fig. 7 by showing the value of ξ corresponding to different interpolation schemes and orders, with respect to the density of the 1D grid Θ_G.

The impact of ρ and ξ on the estimation error depends on the properties of the single-step cost function. Definition 3 translates a first such property by defining parameters related to the jacobian of the transformation $\mathcal{S}$. These enable us to make connections between worst-case errors in the admissible sensing domain $\mathcal{T}$ (defined in (3)) and corresponding errors in the domain of interest $\mathcal{P}$.

Definition 3 (Variations of parameter projection)**.** *The global projection function $\mathcal{S} : \mathcal{P} \mapsto \mathcal{T}$ exhibits the maximal and the minimal variation coefficient, respectively defined by*

$$\bar{\lambda}_\mathrm{min} := \min_{\boldsymbol{p}\in\mathcal{P}} \lambda_\mathrm{min}\big(\boldsymbol{J}(\boldsymbol{p})^\top \boldsymbol{J}(\boldsymbol{p})\big), \tag{27}$$

$$\bar{\lambda}_\mathrm{max} := \max_{\boldsymbol{p}\in\mathcal{P}} \lambda_\mathrm{max}\big(\boldsymbol{J}(\boldsymbol{p})^\top \boldsymbol{J}(\boldsymbol{p})\big), \tag{28}$$

where $\boldsymbol{J}(\boldsymbol{p})$ denotes the jacobian matrix of $\mathcal{S}$ evaluated in $\boldsymbol{p}$.

The quantities $\bar{\lambda}_\mathrm{min}$ and $\bar{\lambda}_\mathrm{max}$ are also related to the injectivity of the global PPF. We emphasize this aspect with the following lemma, proven in Appendix D,

Lemma 1. *Given $\mathcal{S}$, a global PPF, and a* convex *domain $\mathcal{P}$ meeting Assumption 1, if $\bar{\lambda}_\mathrm{min} > 0$ then $\mathcal{S}$ is invertible over $\mathcal{P}$.*

It follows that the ill-posed situation of a non-injective global projection function yields $\bar{\lambda}_\mathrm{min} = 0$. This extreme case suggests that a high value of $\bar{\lambda}_\mathrm{max}$ with a low value of $\bar{\lambda}_\mathrm{min}$ leads to higher estimation errors.

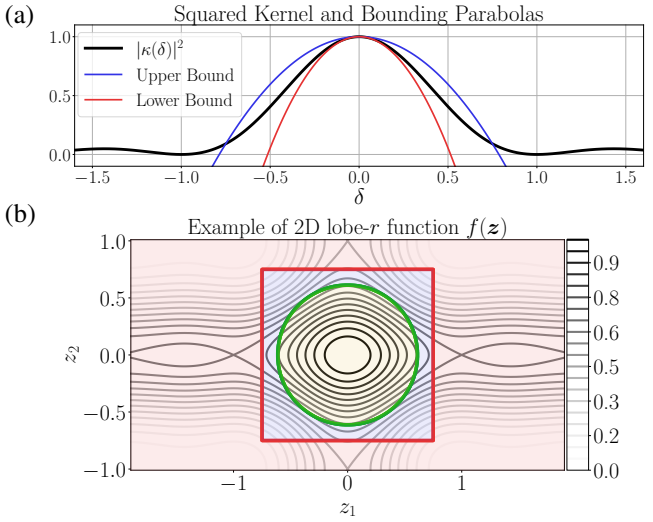

Fig. 8. **(a)** Example of a lobe-r function ($r = .75$) corresponding to the squared kernel $|\kappa(\delta)|^2$ of the atom (12), with a choice of upper and lower bounding parabolas. **(b)** A two-dimensional lobe-r function ($r = .53$) obtained from a weighted outer summation of two functions as depicted in (a). We call the green region the inner-lobe, the blue region the outer-lobe, and the red region the outside.

Finally, the shape of the single-step cost function also depends on the decreasing properties of the squared correlation kernel $|\kappa(\cdot)|^2$ (defined in (5)). We evaluate this aspect by introducing the concept of "lobe-r" functions.

Definition 4 (lobe-r function)**.** *Given $r > 0$ and a domain $\mathcal{Z} \subset \mathbb{R}^n$, a function $f : \mathcal{Z} \mapsto \mathbb{R}$ is said to be lobe-r if there is $R \geq r$ such that for all $\boldsymbol{z}^\mathrm{in} \in \mathbb{B}_2(r)$ and for all $\boldsymbol{z}^\mathrm{out} \in \mathcal{Z}\backslash\mathbb{B}_\infty(R)$, we have*

$$f(\boldsymbol{z}^\mathrm{in}) > f(\boldsymbol{z}^\mathrm{out}), \tag{29}$$

and if there are positive lobe-bounding constants $0 < U \leq L$ such that for all $\boldsymbol{z} \in \mathbb{B}_\infty(R)$, the following holds

$$1 - L\|\boldsymbol{z}\|_2^2 \leq f(\boldsymbol{z}) \leq 1 - U\|\boldsymbol{z}\|_2^2. \tag{30}$$

In particular, all the above imply that $f(\boldsymbol{z})$ has a unique global maximizer $\boldsymbol{z} = \boldsymbol{0}$, with $f(\boldsymbol{0}) = 1$.

This concept can be better understood by inspecting Fig. 8. More precisely, Fig. 8(a) shows an example of a lobe-r function with its lower and upper bounding parabolas that illustrate the condition (30). In Fig. 8(b), a 2D lobe function is given with regions highlighted in different colors. We respectively call the *inner-lobe* and the *outer-lobe* of f, the domains $\mathbb{B}_2(r)$ and $\mathbb{B}_\infty(R)\backslash\mathbb{B}_2(r)$. The property (29) tells us that any value of f taken inside the inner lobe is greater than all evaluations of f outside the outer lobe. For $\boldsymbol{z} \in \mathbb{B}_\infty(R)\backslash\mathbb{B}_2(r)$, $f(\boldsymbol{z})$ may take values larger than inside the inner lobe but follows the decreasing rule (30).

We note that the squared kernel $|\kappa(\cdot)|^2$ resulting from any of the examples given in Sec. V is a lobe-r function for some $r > 0$. Practically speaking, the inner radius r of $|\kappa(\cdot)|^2$ is then closely related to the sensor resolution.

B. The Grid Hopping Estimation Bound

Using the definitions above, we present here our main theoretical result in Theorem 1. In the following, we use a notation for normalized amplitude coefficients (defined in (4)),

$$\gamma_q = |\alpha_q|^2 \,/\, \textstyle\sum_{q'=0}^{Q} |\alpha_{q'}|^2, \tag{31}$$

and we set $\gamma_{\max} := \max_{q\in[Q]} \gamma_q$, $\gamma_{\min} := \min_{q\in[Q]} \gamma_q$.

Theorem 1 (Grid Hopping Estimation Bound)**.** *Assuming that*

- *(A.1) the grid $\mathcal{P}_{\mathrm{G}}$ discretizes $\mathcal{P}$ with a covering radius ρ,*
- *(A.2) we use an interpolation scheme with a gap ξ,*
- *(A.3) the atom function $\boldsymbol{a}$ defines a translation invariant kernel such that $|\kappa(\cdot)|^2$ is a lobe-r function with L, U as lower and upper bounding constants,*

and given measurements provided by (4) *with* no noise*, the following error bound on the estimate $\hat{\boldsymbol{p}}$ resulting from the estimation* (19) *holds: With the constants*

$$R_{\mathrm{P}} := \sqrt{\tfrac{L\gamma_{\max}}{U\gamma_{\min}}}, \quad \tilde{U} := U\gamma_{\min}, \quad \tilde{R}_{\mathrm{P}} := \tfrac{(4R_{\mathrm{P}}+\sqrt{2})}{\sqrt{\tilde{U}}}, \tag{32}$$

if

$$(\bar{\lambda}_{\max} R_{\mathrm{P}}^2)\, \rho^2 \,+\, \tfrac{2\sqrt{2}}{\tilde{U}}\, \xi \,\leq\, r^2, \tag{33}$$

then

$$\|\hat{\boldsymbol{p}} - \boldsymbol{p}^*\|_2 \leq \bar{\lambda}_{\min}^{-\frac{1}{2}} \big(\tilde{R}_{\mathrm{P}}\, \xi \,+\, \bar{\lambda}_{\max}^{\frac{1}{2}} R_{\mathrm{P}}\, \rho\big). \tag{34}$$

Theorem 1 is proven in the appendix. In words, if the covering radius ρ of $\mathcal{P}_{\mathrm{G}}$ is sufficiently smaller than the inner lobe r, then the noiseless estimation error $\|\hat{\boldsymbol{p}} - \boldsymbol{p}^*\|_2$ is upper bounded by a weighted sum of the interpolation gap ξ and the covering radius ρ.

As announced at the beginning of this section, we can particularize our bound for two scenarios. In a standard single-step estimation with no GH, and hence the only error is the *gridding error*, proportional to ρ according to (34) with $\xi = 0$. If, on the other hand, GH is used to estimate $\boldsymbol{p}$ in a continuous space (*e.g.*, with an infinitely dense grid $\mathcal{P}_{\mathrm{G}}$), then $\rho = 0$ and only the interpolation error, proportional to ξ, remains.

C. Discussion on the GH Estimation Bound

We now proceed to analyze the insights we can learn from our bound. We first highlight that the factor $\bar{\lambda}_{\min}^{-\frac{1}{2}}$ translates the impact of the "geometry" of the scenario and the network's ability to observe the parameter of interest diversely, inherently embodied in the properties of the PPF. Notably, the ill-conditioned network with $\bar{\lambda}_{\min} = 0$ studied by Lem. 1 yields an unbounded error.

In addition, since R_{P} is minimized when all the received signals exhibit similar power (*i.e.*, $\gamma_{\max} = \gamma_{\min}$), our bound suggests that imbalance between the power levels of the signals negatively impacts the estimation performance in single-step methods.

The bound also enables us to study the impacts of using either a dense grid or a higher-order interpolation scheme. We remind the reader that GH's computational complexity is proportional to $N_\Theta M + N_{\mathrm{P}} I$. If the term in ρ dominates the error, we can only decrease ρ to significantly improve the performance, thereby increasing N_{P}. If, however, the term in ξ dominates, we can decrease this term either by using a more precise interpolation scheme (*e.g.*, a polar interpolation instead of ZOH) or by increasing the density of the grid Θ_{G}. Computationally, in the first case, we increase I; in the other case, we increase N_Θ. Therefore, determining the best choice between these two ways of decreasing ξ depends on the value of N_{P}. If $N_\Theta M$ dominates the computation time, a higher-order interpolation scheme is preferred. If $N_{\mathrm{P}} I$ dominates, a low-order interpolation scheme with a denser grid Θ_{G} is preferred. This effect will be observed in the numerical results.

Finally, while our bound studies the joint impact of the discretization of $\mathcal{P}_{\mathrm{G}}$ and the interpolation on the estimation error, its deterministic point of view makes it a separated approach from standard bounds on the effect of the noise, such as the CRLB. We postpone the in-depth study of the joint effect of the three sources of errors we listed at the beginning of this section for a future dedicated publication. In particular, the derivation of a CRLB, taking into account the effect of the gridding and interpolation errors as equivalent noise in the estimate, in a similar fashion as quantization noise, is expected to add a valuable contribution in the future to understand the interconnection between those aspects.

VIII. Numerical Results

This section presents numerical results from extensive Monte-Carlo simulations. First, we compare the bound from Sec. VII with simulation results on the simple MSR application of Fig. 5, in a noiseless scenario that fits the conditions for which Thm. 1 applies. These results, presented in Sec. VIII-A, compare our theoretical worst-case error bound with corresponding worst-case errors observed in numerical experiments, thereby showing the bound's level of tightness.

Next, in Sec. VIII-B, we assess the effectiveness of GH in connection with the choice of interpolation scheme, using simulations performed for two different applications. These results highlight how GH can augment single-step estimation algorithms by significantly reducing their computational complexity while maintaining efficiency and only inducing minimal estimation inaccuracy.

A. Evaluation of the GH Bound

We randomly selected 10,000 realizations for the value of the true parameter of interest $\boldsymbol{p}^*$, taken following a uniform distribution in $\mathcal{P}$, depicted in Fig. 5(a). For each selected value of $\boldsymbol{p}^*$, we computed the collection of Q noiseless and equal-power measurements $\{\boldsymbol{y}_q\}_{q=1}^{Q}$ (*i.e.*, with $\gamma_{\min} = \gamma_{\max} = 1/Q$). For each realization, GH was used with all the interpolation schemes compared in Fig. 7 to obtain estimates $\hat{\boldsymbol{p}}$ of $\boldsymbol{p}^*$. These estimations were performed for several *uniform* griddings Θ_{G} of Θ and griddings $\mathcal{P}_{\mathrm{G}}$ of $\mathcal{P}$. The grids $\mathcal{P}_{\mathrm{G}}$ all have a similar structure as the grid from Fig. 5(a) and are defined with different spacing between adjacent bins, which is directly proportional to the covering radius ρ.

For each grid and interpolation scheme, we recorded the realization which provided the worst (higher) estimation squared error $\|\hat{\boldsymbol{p}} - \boldsymbol{p}^*\|_2^2$. This metric is used here to evaluate the ability of our upper bound to properly translate the behavior

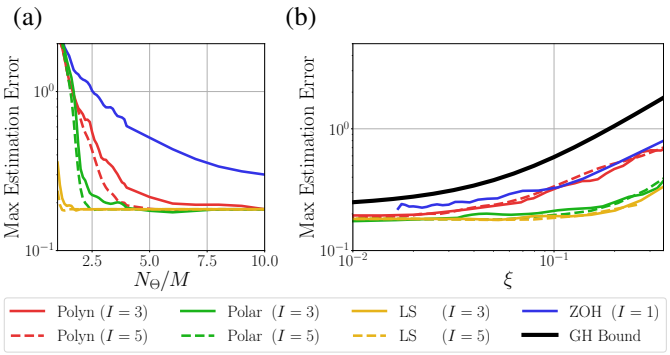

Fig. 9. **(a)** Maximal squared error $\|\hat{\boldsymbol{p}} - \boldsymbol{p}^*\|_2^2$ observed over 10,000 realizations of $\boldsymbol{p}^*$ for multiple interpolation schemes used in GH. **(b)** The same data as (a), with respect to the interpolation gap ξ, obtained from Fig. 7.

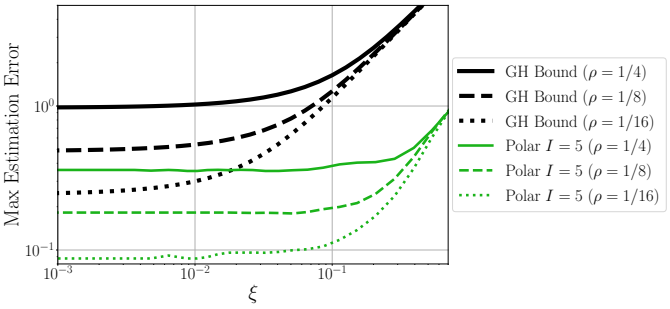

Fig. 10. Comparison of the GH bound with the maximal squared error $\|\hat{\boldsymbol{p}} - \boldsymbol{p}^*\|_2^2$ obtained using GH with the order-5 polar interpolation [53]. Three distinct uniform grids $\mathcal{P}_\mathrm{G}$, characterized by their covering radius ρ are shown.

of the error it is intended to bound. The next section compares performance in detail using an average error metric. Fig. 9(a) depicts these worst-case errors with respect to the density of Θ_G expressed by N_Θ/M, while the grid $\mathcal{P}_\mathrm{G}$ is fixed with $\rho = 1/8$. The comparison with Fig. 7 confirms that the interpolation schemes with lower gaps ξ lead to lower worst-case errors. Increasing N_Θ decreases the error, following the value of ξ shown in Fig. 7 before reaching the grid error resulting from the limited density of the grid $\mathcal{P}_\mathrm{G}$.

In Fig. 9(b), the same data as Fig.9(a) are shown, with respect to the values of ξ taken from Fig. 7. We added the GH bound computed with the fixed covering radius $\rho = 1/8$. Similar results, restricted to the polar interpolation, are depicted in Fig. 10 for multiple values of ρ. We observe two regimes in each curve. The left flat part corresponds to values of ξ such that E_G dominates E_I while the right increasing part corresponds to the regime where E_I dominates. The same two regimes with similar slopes appear in the simulated results. The vertical shift between the theoretical bound and the results is caused by a constant coefficient. In contrast, the horizontal shift translates a mismatch between the theoretical and the actual weightings of ρ and ξ in the expression of the bound. Those are due to the unlikeliness of all the intermediate inequalities used in the derivation of the bound to be tight in a single value of $\boldsymbol{p}^*$. Still, the weighted-sum property of ρ and ξ is preserved when moving from the theory to the simulations.

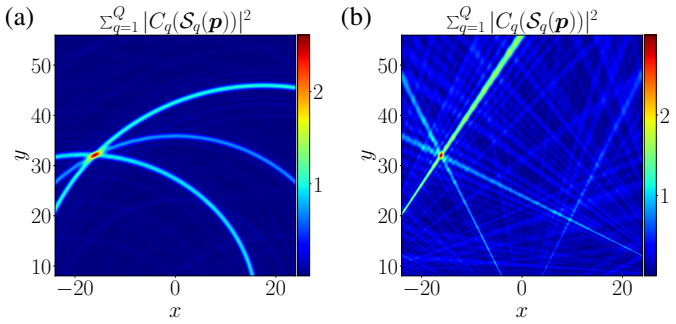

Fig. 11. Correlation functions used in the single-step method (9) on a signal obtained with the two systems simulated in Sec. VIII-B, observing a single target or a signal source located in $\boldsymbol{p}^* = (-16, 32)^\top$ with a SNR = 20dB. **(a)** the MSR system. **(b)** the DoA-based localization system.

B. Grid-Hopping Performance

We validate, on two different systems, the performance of GH in comparison to the single-step and two-step methods presented in Sec. IV. While multiple contributions have already shown the superiority of single-step methods over their two-step counterpart under sophisticated nuisance [19], [24], [25], we restrict our study to the robustness of the GH estimation against white noise. This simple case enables us to highlight the ability of GH to attain performance comparable to those of single-step methods with a computational complexity closer to two-step methods, as well as deriving a rule of thumb to choose the most appropriate interpolation scheme.

The first application is a MSR with $Q = 3$ receivers and a geometry similar to the one presented in Fig. 5(a) with different scales. More precisely, all dimensions are multiplied by 8 and each antenna provides $M = 64$ samples. The other application is a network of sensor arrays as described in Sec. V-C. The receiver nodes are located in the same location as the receivers of the MSR described above, and each node is a circular array of sub-receivers, as used in [63], whose radius is 16λ and composed of $M = 64$ receivers. Examples of correlation functions computed by a single-step method in both setups are given in Fig. 11.

Simulating the MSR system for multiple values of Signal-to-Noise Ratio (SNR), we averaged the estimation error $\|\hat{\boldsymbol{p}} - \boldsymbol{p}^*\|_2$ over 10,000 realizations of signals (see model 4) in which $\boldsymbol{p}^*$ have been taken uniformly at random in $\mathcal{P}$ and the coefficients α_q have been taken independently for each index q from a complex normal distribution of variance equal to 1. Fig. 12(a) shows the resulting performance with a covering radius $\rho = 1/4$, when $N_\Theta/M = 4$. The results confirm the single-step method's stronger robustness against noise. At a high SNR, the performance saturates, as it reaches the limitation due to the gridding $\mathcal{P}_\mathrm{G}$. The GH curves follow the one of the single-step but saturate sooner to reach, at high SNR, a performance which depends on the choice of interpolation. The ZOH strategy logically yields the worst GH performance, while higher order interpolations exhibit here performance almost indistinguishable from the single-step algorithm.

Fig. 12(b)-(c) respectively show the average estimation error and the computation time with respect to the cardi-

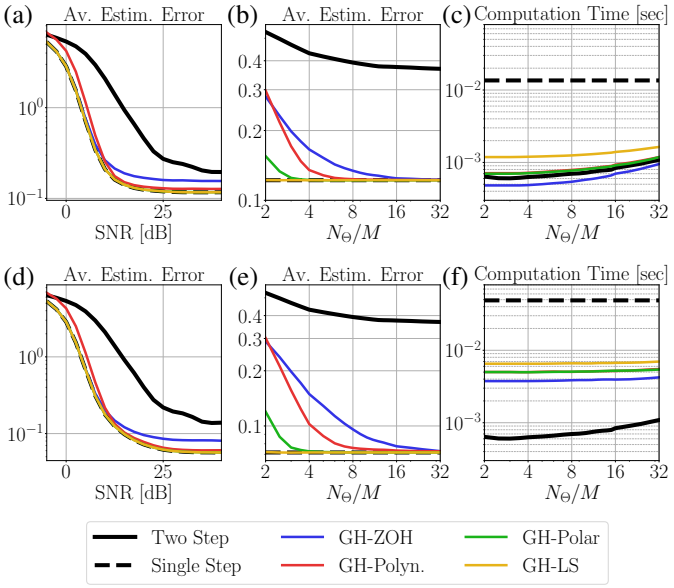

Fig. 12. Simulation results from the MSR system showing the average of the estimation error $\|\hat{\boldsymbol{p}} - \boldsymbol{p}^*\|_2$ over 10,000 realization of noisy signals following (4). The polynomial, the polar, and the LS interpolator used in GH for this simulation are all of order $I = 3$. Two different distinct uniform grids $\mathcal{P}_\mathrm{G}$ are used. In **(a)-(c)**, covering radius $\rho = 1/4$ and in **(d)-(f)**, $\rho = 1/8$.

nality N_Θ of Θ_G with a constant 20dB SNR. For a given interpolation scheme, increasing N_Θ leads to smaller errors, but increases the GH's computation time. In the considered scenario, the term in $N_\Theta M$ dominates the computation time of GH methods. The polar interpolation with $N_\Theta/M = 4$ thus appears as the potential best compromise between the performance and the computation time. The LS interpolator requires a higher computation time than the polar one because it requires complex interpolating coefficients and, hence, is computationally of order $I = 6$ instead of 3.

Fig. 12(d)-(f), shows similar results for $\rho\ \mathcal{P}_\mathrm{G}$ equal to $1/8$. The same conclusions as before apply but the computation times tell another story. Since the number of grid bins N_P has increased, the term in $N_\mathrm{P} I$ now dominates the computation time. It is now more efficient to reduce ξ by increasing N_Θ instead of I. Practically, this translates into the conclusion that the ZOH strategy with a dense sensed grid Θ_G is the best compromise between performance and computation time.

This observation confirms the intuition described in Sec. VII and provided by the GH bound. In short, when N_P is sufficiently small, then a higher order interpolation is preferred to reach the single-step method's performance with GH. As N_P becomes larger, using a lower order interpolation with a dense sensing grid Θ_G becomes computationally more efficient.

Finally, Fig. 13 shows similar results when applied to the second application. Since the atom function described by (16) is not translation invariant, we can no longer use the polar interpolation for which this property is a requirement. Also, this implies that our theoretical bound is no longer ensured. Still, the observation of similar results as for the MSR system tends to assume that the main intuition provided by the bound can be extended beyond the translation-invariance assumption.

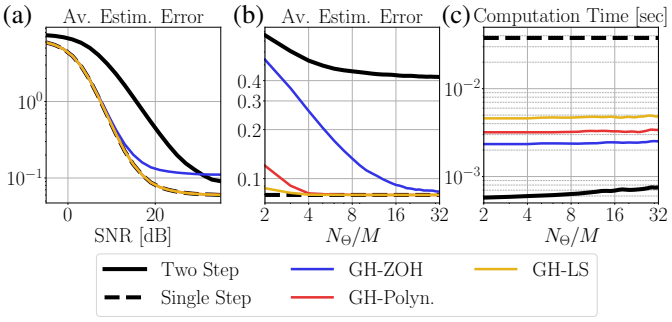

Fig. 13. Simulation results from the DoA-based localization system, similar as Fig. 12, for a grid $\mathcal{P}_\mathrm{G}$ with $\rho = 1/8$.

IX. Conclusion

This paper intends to introduce and evaluate the Grid Hopping framework, which generalizes multiple acceleration techniques of single-step estimation methods for networks of sensors. With a few assumptions on the system and the sensing scenario, we provided a theoretical bound on the estimation error between the GH estimate and the ground truth. We used our bound to derive a rule indicating the situations where using a lower order interpolation with a dense grid is expected to be computationally more efficient than using a high order interpolating with coarse grids for similar performance. With the Monte-Carlo simulation, we confirmed the intuitive rule and showed the effectiveness of GH in simple sensing scenarios.

While this paper focused on presenting and characterizing the GH framework in its simplest applicative context, future research includes the application of GH to more advanced single-step algorithms tailored for the estimation of multiple parameters of interest and including off-grid search or refinement of the estimates, as well as further evaluations of the method in systems that suffer from additional non-idealities such as reverberation. When integrating these advanced algorithms with GH, comparing their resulting performance with the CRLB is expected to provide insight into the level of degradation introduced by the use of GH. Therefore, deriving CRLB specifically tailored to take into account this degradation is another possible key direction for future research built upon our results.

Appendix

This appendix is dedicated to the proof of Theorem 1. This proof is structured on the basis that Theorem 1 results from a particularization of simpler and a more general theorem: Theorem 2. This theorem bounds the norm of the maximizer of a function $\tilde{f}$ approximating a lobe-r function f.

More precisely, we organize the appendix as follows. First, Appendix A describes, proves, and interprets the more general Theorem 2 from which Theorem 1 originates. Next, we provide in Appendix B three technical lemmas required to apply Theorem 2 in the specific context of interest for our bound, *i.e.*, the GH's optimization problem (19). Finally, Appendix C exploits all the above to effectively prove Theorem 1.

A. Approximate Lobe Function Maximization Bound

The maximizer of a lobe-r function f is trivially 0 by definition of this concept. In contrast, Theorem 2 bounds the "error" (compared to 0) one obtains when maximizing an approximate function $\tilde{f}$ instead, and when this optimization is moreover constrained in a subset of the domain of f. To bound this error, this theorem exploits the decreasing properties of the lobe-r function f.

In the proof of Theorem 1, we will match the GH optimization (19) with the optimization problem studied by Theorem 2. Note that the distinction of the two constants η and η' in this theorem has importance for the derivation of Theorem 1.

Theorem 2 (Lobe Function Maximization Bound)**.** *Let $\tilde{f} : \mathcal{Z} \mapsto \mathbb{R}$ be an approximation of the lobe-r function f such that for all $\boldsymbol{z} \in \mathcal{Z}$,*

$$|\tilde{f}(\boldsymbol{z}) - f(\boldsymbol{z})| \leq \eta. \tag{35}$$

Given a set $\mathcal{Z}' \subset \mathcal{Z}$ and $\boldsymbol{z}_{\mathrm{ref}} \in \arg\min_{\boldsymbol{z}\in\mathcal{Z}'} \|\boldsymbol{z}\|_2$, if

$$\|\boldsymbol{z}_{\mathrm{ref}}\|_2^2 < \tfrac{Ur^2-2\eta}{L}, \tag{36}$$

then the estimate $\hat{\boldsymbol{z}}$ defined by

$$\hat{\boldsymbol{z}} := \operatorname*{arg\,max}_{\boldsymbol{z}\in\mathcal{Z}'} \tilde{f}(\boldsymbol{z}) \tag{37}$$

is such that

$$\|\hat{\boldsymbol{z}}\|_2^2 \leq \frac{L}{U}\|\boldsymbol{z}_{\mathrm{ref}}\|_2^2 + \frac{2}{U}\,\eta', \tag{38}$$

where η' is a constant potentially smaller than η such that $|\tilde{f}(\boldsymbol{z}) - f(\boldsymbol{z})| \leq \eta'$ holds specifically *for $\boldsymbol{z} \in \{\boldsymbol{z}_{\mathrm{ref}}, \hat{\boldsymbol{z}}\}$.*

Proof. To exploit the decreasing property (30) of the lobe-r function f and thereby prove Theorem 2, we must first guarantee that $\hat{\boldsymbol{z}}$ belongs inside the outer lobe, *i.e.*, $\hat{\boldsymbol{z}} \in \mathbb{B}_\infty(R)$. This is directly proven if we show that for all $\boldsymbol{z}^{\mathrm{out}} \in \mathcal{Z}\backslash\mathbb{B}_\infty(R)$, we always have $\tilde{f}(\hat{\boldsymbol{z}}) > \tilde{f}(\boldsymbol{z}^{\mathrm{out}})$.

We demonstrate this inequality by first rewriting (36) as

$$1 - L\|\boldsymbol{z}_{\mathrm{ref}}\|_2^2 - \eta > 1 - Ur^2 + \eta. \tag{39}$$

Next, we upper bound the left part of (39) by applying (30) in $\boldsymbol{z}_{\mathrm{ref}}$. We can do this since $L \geq U$ and $\eta \geq 0$ by definition, and hence the constraint (36) ensures $\|\boldsymbol{z}_{\mathrm{ref}}\|_2 < r$.

We also lower bound the right part of (39) by noticing that for all $\boldsymbol{z}^{\mathrm{out}} \in \mathcal{Z}\backslash\mathbb{B}_\infty(R)$, it holds $f(\boldsymbol{z}^{\mathrm{out}}) \leq 1 - Ur^2$. Indeed, by the decreasing property (30), any $\boldsymbol{z}^{\mathrm{in}}$ such that $\|\boldsymbol{z}^{\mathrm{in}}\|_2 = r$ provides $f(\boldsymbol{z}^{\mathrm{in}}) \leq 1 - Ur^2$, while following the property (29), we have $f(\boldsymbol{z}^{\mathrm{out}}) \leq f(\boldsymbol{z}^{\mathrm{in}})$.

Applying the above to (39), it results

$$f(\boldsymbol{z}_{\mathrm{ref}}) - \eta > f(\boldsymbol{z}^{\mathrm{out}}) + \eta, \tag{40}$$

for all $\boldsymbol{z}^{\mathrm{out}} \in \mathcal{Z}\backslash\mathbb{B}_\infty(R)$. Using (35), we conclude that $\tilde{f}(\boldsymbol{z}_{\mathrm{ref}}) > \tilde{f}(\boldsymbol{z}^{\mathrm{out}})$ and hence $\hat{\boldsymbol{z}} \in \mathbb{B}_\infty(R)$.

With the above, we showed that we can apply (30) on both $f(\boldsymbol{z}_{\mathrm{ref}})$ and $f(\hat{\boldsymbol{z}})$. Combined with the definition of η', this leads to

$$\tilde{f}(\hat{\boldsymbol{z}}) \leq f(\hat{\boldsymbol{z}}) + \eta' \leq 1 - U\|\hat{\boldsymbol{z}}\|_2^2 + \eta', \tag{41}$$

and

$$\tilde{f}(\boldsymbol{z}_{\mathrm{ref}}) \geq f(\boldsymbol{z}_{\mathrm{ref}}) - \eta' \geq 1 - L\|\boldsymbol{z}_{\mathrm{ref}}\|_2^2 - \eta'. \tag{42}$$

Since $\tilde{f}(\hat{\boldsymbol{z}}) \geq \tilde{f}(\boldsymbol{z}_{\mathrm{ref}})$, this implies $\|\hat{\boldsymbol{z}}\|_2^2 \leq \frac{L}{U}\|\boldsymbol{z}_{\mathrm{ref}}\|_2^2 + \frac{2}{U}\eta'$ and concludes the proof. □

B. Auxilliary lemmas

Showing how the context of the GH estimation fits the one of Theorem 2 requires a few technical lemmas.

We begin with a lemma showing that a positive weighted sum of the lobe-r function is also a lobe-$\tilde{r}$ function, described by an inner radius and bounding constants that depend on the sum's weights. This lemma is helpful to characterize properties of the objective function of (19) and to show that it meets the conditions for Theorem 2.

Lemma 2 (Summation of lobes)**.** *Given positive $b_1, \cdots, b_Q$ such that $\sum_{q\in[Q]} b_q = 1$ and the separable function*

$$f_{\mathrm{b}} \ : \ \mathcal{Z}^Q \mapsto \mathbb{R} \ : \ f_{\mathrm{b}}(\boldsymbol{z}) = \textstyle\sum_{q\in[Q]} b_q f(\boldsymbol{z}_q), \tag{43}$$

with f a lobe-r function and $\boldsymbol{z} = [\boldsymbol{z}_1^\top, \cdots, \boldsymbol{z}_Q^\top]^\top$, f_{b} is lobe-$\tilde{r}$ whose lobe is bounded by $\tilde{L}$ and $\tilde{U}$ obtained from

$$\tilde{r}^2 = \tfrac{U}{L}\tfrac{b_{\min}}{b_{\max}} r^2, \quad \tilde{L} = L b_{\max}, \quad \tilde{U} = U b_{\min}, \tag{44}$$

and where $b_{\max} := \max_{q\in[Q]} b_q$ and $b_{\min} := \min_{q\in[Q]} b_q$.

Proof. For this proof, we use the notation $\bar{\mathbb{B}}_p(r) := \{\boldsymbol{z} \in \mathcal{Z}^Q : \|\boldsymbol{z}\|_p \leq r\}$, while the ball $\mathbb{B}_p(r)$ is defined in $\mathcal{Z}$. We first prove that property (29) holds for f_{b} with $\tilde{r}$ defined by (44). To this end, let us define

$$\boldsymbol{z}^{\mathrm{in}} := [(\boldsymbol{z}_1^{\mathrm{in}})^\top, \cdots, (\boldsymbol{z}_Q^{\mathrm{in}})^\top]^\top, \tag{45}$$

$$\boldsymbol{z}^{\mathrm{out}} := [(\boldsymbol{z}_1^{\mathrm{out}})^\top, \cdots, (\boldsymbol{z}_Q^{\mathrm{out}})^\top]^\top. \tag{46}$$

such that $\boldsymbol{z}^{\mathrm{out}} \in \mathcal{Z}^Q\backslash\bar{\mathbb{B}}_\infty(R)$ and that $\boldsymbol{z}_q^{\mathrm{in}} \in \mathbb{B}_2(r)$ for all $q \in [Q]$. By construction, there is at least one index $q' \in [Q]$ such that $\boldsymbol{z}_{q'}^{\mathrm{out}} \in \mathcal{Z}\backslash\mathbb{B}_\infty(R)$. For such index q', the properties of a lobe-r function guarantee that

$$f(\boldsymbol{z}_{q'}^{\mathrm{out}}) < \min_{\boldsymbol{z}\in\mathbb{B}_2(r)} f(\boldsymbol{z}) \leq 1 - U \max_{\boldsymbol{z}\in\mathbb{B}_2(r)} \|\boldsymbol{z}\|_2^2 = 1 - Ur^2. \tag{47}$$

For other indexes $q \neq q'$, we have $f(\boldsymbol{z}_q^{\mathrm{out}}) \leq 1$ since 1 is the maximum value of f by definition. Therefore,

$$f_{\mathrm{b}}(\boldsymbol{z}^{\mathrm{out}}) < 1 - b_{q'} Ur^2 \leq 1 - b_{\min} Ur^2. \tag{48}$$

Moreover, using property (30), we have

$$f_{\mathrm{b}}(\boldsymbol{z}^{\mathrm{in}}) \geq \textstyle\sum_{q\in[Q]} b_q (1 - L\|\boldsymbol{z}_q^{\mathrm{in}}\|_2^2) \tag{49}$$

$$= 1 - \textstyle\sum_{q\in[Q]} b_q L \|\boldsymbol{z}_q^{\mathrm{in}}\|_2^2 \tag{50}$$

$$\geq 1 - b_{\max} L \|\boldsymbol{z}^{\mathrm{in}}\|_2^2. \tag{51}$$

From (48) and (51), we deduce that any couple ($\boldsymbol{z}^{\mathrm{in}}$, $\boldsymbol{z}^{\mathrm{out}}$) defined as above exhibits the inequality

$$f_{\mathrm{b}}(\boldsymbol{z}^{\mathrm{in}}) - f_{\mathrm{b}}(\boldsymbol{z}^{\mathrm{out}}) > b_{\min} Ur^2 - b_{\max} L \|\boldsymbol{z}^{\mathrm{in}}\|_2^2. \tag{52}$$

A sufficient condition for $f_{\mathrm{b}}(\boldsymbol{z}^{\mathrm{in}}) - f_{\mathrm{b}}(\boldsymbol{z}^{\mathrm{out}})$ to be positive is $\|\boldsymbol{z}^{\mathrm{in}}\|_2^2 \leq \frac{U}{L}\frac{b_{\min}}{b_{\max}} r^2 := \tilde{r}^2$, which proves (44).

Now we prove that the bounding property (30) holds for f_{b} with $\tilde{L}$ and $\tilde{U}$. For all $\boldsymbol{z} = [\boldsymbol{z}_1^\top, \cdots, \boldsymbol{z}_Q^\top]^\top \in \bar{\mathbb{B}}_\infty(R) \subset \mathcal{Z}^Q$, we necessarily have $\boldsymbol{z}_q \in \mathbb{B}_\infty(R) \subset \mathcal{Z}$ for all $q \in [Q]$.

Therefore, we can apply (30) separately to each term of the summation (43) to obtain

$$f_{\mathrm{b}}(\boldsymbol{z}) \geq 1 - \textstyle\sum_{q\in[Q]} b_q L \|\boldsymbol{z}_q\|_2^2 \geq 1 - b_{\max} L \|\boldsymbol{z}\|_2^2 \quad (53)$$

$$f_{\mathrm{b}}(\boldsymbol{z}) \leq 1 - \textstyle\sum_{q\in[Q]} b_q U \|\boldsymbol{z}_q\|_2^2 \leq 1 - b_{\min} U \|\boldsymbol{z}\|_2^2, \quad (54)$$

which proves (44) and concludes this proof. □

Next, we provide a lemma that will help us in bounding the error between the exact sum of squared correlations appearing in (9) with the approximation used by GH in (19).

Lemma 3. *Given three vectors $\boldsymbol{v}_1, \boldsymbol{v}_2$ and $\boldsymbol{v}_3$ with unit ℓ_2 norm and two positive constants ε and η such that*

$$|\langle \boldsymbol{v}_1, \boldsymbol{v}_2\rangle|^2 \geq 1-\varepsilon^2 \quad \textit{and} \quad |\langle \boldsymbol{v}_1, \boldsymbol{v}_3\rangle|^2 \geq 1-\eta^2, \quad (55)$$

two inequalities hold

$$\big||\langle \boldsymbol{v}_1, \boldsymbol{v}_3\rangle|^2 - |\langle \boldsymbol{v}_2, \boldsymbol{v}_3\rangle|^2\big| \leq \sqrt{2}\varepsilon, \quad (56)$$

$$\big||\langle \boldsymbol{v}_1, \boldsymbol{v}_3\rangle|^2 - |\langle \boldsymbol{v}_2, \boldsymbol{v}_3\rangle|^2\big| \leq 2\varepsilon\eta + \varepsilon^2. \quad (57)$$

Proof. For this proof, we use the notation $\boldsymbol{V}_i = \boldsymbol{v}_i \boldsymbol{v}_i^H$ for $i \in \{1,2,3\}$ and $\langle , \rangle_{\mathrm{F}}$ as the Frobenius inner product. The left part of (56) and (57) is thus equivalent to $\big|\langle \boldsymbol{V}_1 - \boldsymbol{V}_2, \boldsymbol{V}_3\rangle_{\mathrm{F}}\big|$.

To prove (56), we apply the Cauchy-Scharwz inequality,

$$\big|\langle \boldsymbol{V}_1 - \boldsymbol{V}_2, \boldsymbol{V}_3\rangle_{\mathrm{F}}\big| \leq \|\boldsymbol{V}_1 - \boldsymbol{V}_2\|_{\mathrm{F}} \|\boldsymbol{V}_3\|_{\mathrm{F}}. \quad (58)$$

Since $\|\boldsymbol{V}_i - \boldsymbol{V}_j\|_{\mathrm{F}}^2 = 2 - 2|\langle \boldsymbol{v}_i, \boldsymbol{v}_j\rangle|^2$ and $\|\boldsymbol{V}_3\|_{\mathrm{F}} = 1$, injecting (55) in the above provides (56).

The inequality (57) is similarly proven by developing $\big|\langle \boldsymbol{V}_1 - \boldsymbol{V}_2, \boldsymbol{V}_3\rangle_{\mathrm{F}}\big|$ as

$$\begin{aligned}&\big|\langle \boldsymbol{V}_1 - \boldsymbol{V}_2, \boldsymbol{V}_1 - \boldsymbol{V}_3\rangle_{\mathrm{F}} - \langle \boldsymbol{V}_1 - \boldsymbol{V}_2, \boldsymbol{V}_1\rangle_{\mathrm{F}}\big| \\ &\quad \leq \|\boldsymbol{V}_1 - \boldsymbol{V}_2\|_{\mathrm{F}} \|\boldsymbol{V}_1 - \boldsymbol{V}_3\|_{\mathrm{F}} + |1 - \langle \boldsymbol{V}_1, \boldsymbol{V}_2\rangle_{\mathrm{F}}|. \quad (59)\end{aligned}$$

Since $\langle \boldsymbol{V}_1, \boldsymbol{V}_2\rangle_{\mathrm{F}} = |\langle \boldsymbol{v}_1, \boldsymbol{v}_2\rangle|^2$, injecting (55) in the above provides (57). □

We end this tour of technical lemmas with a property enabling us to exploit Definition 3 to navigate from the domain of interest $\mathcal{P}$ to the admissible sensed domain $\mathcal{T}$ and inversely.

Lemma 4. *Given a global PPF following assumption 1 and denoted by $\mathcal{S}$, for all pairs $\boldsymbol{p}_1, \boldsymbol{p}_2 \in \mathcal{P}$ and $\boldsymbol{\theta}_1, \boldsymbol{\theta}_2 \in \mathcal{T}$ such that $\boldsymbol{\theta}_1 = \mathcal{S}(\boldsymbol{p}_1)$ and $\boldsymbol{\theta}_2 = \mathcal{S}(\boldsymbol{p}_2)$, the following holds*

$$\bar{\lambda}_{\min} \|\boldsymbol{p}_2 - \boldsymbol{p}_1\|_2^2 \leq \|\boldsymbol{\theta}_2 - \boldsymbol{\theta}_1\|_2^2 \leq \bar{\lambda}_{\max} \|\boldsymbol{p}_2 - \boldsymbol{p}_1\|_2^2. \quad (60)$$

Proof. From the mean value theorem, $\boldsymbol{\theta}_2 - \boldsymbol{\theta}_1 = \boldsymbol{J}(\boldsymbol{p})(\boldsymbol{p}_2 - \boldsymbol{p}_1)$ for some $\boldsymbol{p} \in \mathcal{P}$. Therefore,

$$\begin{aligned}\|\boldsymbol{\theta}_2 - \boldsymbol{\theta}_1\|_2^2 &= (\boldsymbol{p}_2 - \boldsymbol{p}_1)^\top \boldsymbol{J}^\top(\boldsymbol{p}) \boldsymbol{J}(\boldsymbol{p}) (\boldsymbol{p}_2 - \boldsymbol{p}_1) \\ &\in [\bar{\lambda}_{\min}, \bar{\lambda}_{\max}] \|\boldsymbol{p}_2 - \boldsymbol{p}_1\|_2^2. \quad (61)\end{aligned}$$

□

C. Proof of Theorem 1

Now, we exploit the above lemmas to prove Theorem 1 by applying Theorem 2 to the GH estimation (19).

To help us connect this optimization problem with the formalism of Theorem 2, let us begin this proof by defining some functions derived from the kernel κ (see (5)). Given the ground truth $\boldsymbol{p}^*$ which is sensed through its associated sensed parameters $\boldsymbol{\theta}^* = (\theta_1^*, \cdots, \theta_Q^*)^\top := \mathcal{S}(\boldsymbol{p}^*)$, the approximated kernels, which result from the use of $\tilde{\boldsymbol{a}}$ instead of $\boldsymbol{a}$ in the correlation processes, read for all $q \in [Q]$,

$$\tilde{\kappa}_q(\delta) := \langle \tilde{\boldsymbol{a}}(\theta_q^* + \delta), \boldsymbol{a}(\theta_q^*)\rangle. \quad (62)$$

Next, we consider the summation performed in the single-step method with and without GH respectively in (9) and (19). When particularized to the noiseless context for which this bound applies, and given $\boldsymbol{\delta} := (\delta_1, \cdots, \delta_Q)^\top$, this yields

$$\kappa_\Sigma(\boldsymbol{\delta}) := \textstyle\sum_{q\in[Q]} \gamma_q |\kappa(\delta_q)|^2, \quad (63)$$

$$\tilde{\kappa}_\Sigma(\boldsymbol{\delta}) := \textstyle\sum_{q\in[Q]} \gamma_q |\tilde{\kappa}_q(\delta_q)|^2 \quad (64)$$

Using the definition here above and the notation

$$\hat{\boldsymbol{\delta}} = \hat{\boldsymbol{\theta}} - \boldsymbol{\theta}^*, \quad (65)$$

we can now reformulate the optimization in (19) as equivalent to solve

$$\hat{\boldsymbol{\delta}} = \underset{\boldsymbol{\delta}\in\mathcal{T}_{\mathrm{G}}}{\arg\max}\ \tilde{\kappa}_\Sigma(\boldsymbol{\delta}), \quad (66)$$

where $\mathcal{T}_{\mathrm{G}} := \mathcal{S}(\mathcal{P}_{\mathrm{G}}) - \boldsymbol{\theta}^* \subset \mathcal{T} - \boldsymbol{\theta}^*$, and then apply the bijection $\hat{\boldsymbol{p}} = \mathcal{S}^{-1}(\boldsymbol{\theta}^* + \hat{\boldsymbol{\delta}})$. The next part of this proof consists in demonstrating in three steps that (66) meets the conditions for Theorem 2. These steps provide

1) a proof that $\kappa_\Sigma(\boldsymbol{\delta})$ is a lobe function,
2) an upper bound on $|\tilde{\kappa}_\Sigma(\boldsymbol{\delta}) - \kappa_\Sigma(\boldsymbol{\delta})|$,
3) an upper bound on the ℓ_2 norm of $\boldsymbol{\delta}_{\mathrm{ref}} := \arg\min_{\boldsymbol{\delta}\in\mathcal{T}_{\mathrm{G}}} \|\boldsymbol{\delta}\|_2$,

by respectively using Lemma 2, 3 and 4.

Step 1) Since A.3 imposes that $|\kappa(\delta)|^2$ is a lobe-r function and since $\sum_{q\in[Q]} \gamma_q = 1$ by construction, we can use Lemma 2 to derive the properties of κ_Σ. We conclude that κ_Σ is a lobe-$\tilde{r}$ with lobe-bounding constants $\tilde{L}$ and $\tilde{U}$ defined by

$$\tilde{L} = \gamma_{\max} L, \quad \tilde{U} = \gamma_{\min} U, \qquad \tilde{r} = \sqrt{\tfrac{\gamma_{\min} U}{\gamma_{\max} L}}\, r. \quad (67)$$

Step 2) The definition of the interpolation gap implies, for all $\theta \in \Theta$, that

$$\begin{aligned}\xi^2 \geq \|\tilde{\boldsymbol{a}}(\theta) - \boldsymbol{a}(\theta)\|_2^2 &= 2(1 - \Re\{\langle \tilde{\boldsymbol{a}}(\theta), \boldsymbol{a}(\theta)\rangle\}) \quad (68)\\ &\geq 2(1 - |\langle \tilde{\boldsymbol{a}}(\theta), \boldsymbol{a}(\theta)\rangle|), \quad (69)\end{aligned}$$

which in turn, for all $q \in [Q]$ and for all $\delta \in \Theta - \theta_q^*$, leads to

$$\begin{aligned}|\langle \boldsymbol{a}(\theta_q^* + \delta), \tilde{\boldsymbol{a}}(\theta_q^* + \delta)\rangle|^2 &\geq 1 - \xi^2 + \tfrac{\xi^4}{4} \quad (70)\\ &\geq 1 - \xi^2. \quad (71)\end{aligned}$$

Additionally, the lobe bounding property of $|\kappa(\delta)|^2$ gives

$$|\kappa(\delta)|^2 = |\langle \boldsymbol{a}(\theta_q^* + \delta), \boldsymbol{a}(\theta_q^*)\rangle|^2 \geq 1 - L\delta^2. \quad (72)$$

We now apply Lemma 3 to the above. In the notation of this lemma, $\boldsymbol{v}_1$, $\boldsymbol{v}_2$ and $\boldsymbol{v}_3$ are respectively mapped to $\boldsymbol{a}(\theta_q^* + \delta)$, $\tilde{\boldsymbol{a}}(\theta_q^* + \delta)$ and $\boldsymbol{a}(\theta_q^*)$. It results for all $q \in [Q]$ and for all $\delta \in \Theta - \theta_q^*$,

$$\big||\tilde{\kappa}_q(\delta)|^2 - |\kappa(\delta)|^2\big| \leq \min\big\{\sqrt{2}\xi, 2\sqrt{L}\xi|\delta| + \xi^2\big\}. \quad (73)$$

We end this step by extending the above to the sum $\tilde{\kappa}_\Sigma$. For all $\boldsymbol{\delta} \in \mathcal{T} - \boldsymbol{\theta}^*$, we have

$$\begin{aligned}|\tilde{\kappa}_\Sigma(\boldsymbol{\delta}) - \kappa_\Sigma(\boldsymbol{\delta})| &= \big|\textstyle\sum_{q\in[Q]} \gamma_q(|\tilde{\kappa}_q(\delta_q)|^2 - |\kappa(\delta_q)|^2)\big| \\ &\leq \textstyle\sum_{q\in[Q]} \gamma_q\big||\tilde{\kappa}_q(\delta_q)|^2 - |\kappa(\delta_q)|^2\big| \\ &\leq \textstyle\sum_{q\in[Q]} \gamma_q \min\big\{\sqrt{2}\xi, 2\sqrt{L}\xi|\delta_q| + \xi^2\big\} \\ &\leq \min\big\{\sqrt{2}\xi, 2\sqrt{\tilde{L}}\xi\|\boldsymbol{\delta}\|_2 + \xi^2\big\}, \quad (74)\end{aligned}$$

where the last inequality exploits the property $\sum_{q\in[Q]} \gamma_q = 1$, which implies $\sum_{q\in[Q]} \gamma_q|\delta_q| \leq \gamma_{\max}^{\frac{1}{2}}\|\boldsymbol{\delta}\|_2$.

Step 3) The statement A.1 guarantees the existence of $\boldsymbol{p}_{\rm ref} \in \mathcal{P}_{\rm G}$ such that $\|\boldsymbol{p}_{\rm ref} - \boldsymbol{p}^*\|_2^2 \leq \rho^2$. Applying Lemma 4, we have

$$\|\mathcal{S}(\boldsymbol{p}_{\rm ref}) - \boldsymbol{\theta}^*\|_2^2 \leq \bar{\lambda}_{\max}\rho^2. \quad (75)$$

Since by construction, $\mathcal{S}(\boldsymbol{p}_{\rm ref}) - \boldsymbol{\theta}^* \in \mathcal{T}_{\rm G}$, we have $\boldsymbol{\delta}_{\rm ref} := \arg\min_{\boldsymbol{\delta}\in\mathcal{T}_{\rm G}} \|\boldsymbol{\delta}\|_2$ such that

$$\|\boldsymbol{\delta}_{\rm ref}\|_2^2 \leq \bar{\lambda}_{\max}\rho^2 \quad (76)$$

This completes the three steps enabling us to apply Theorem 2 to the maximization (66). Following our conclusion in (74), we map the term η (in the notation of Theorem 2) to $\sqrt{2}\xi$. The term η' is mapped to $2\sqrt{L}\xi\|\hat{\boldsymbol{\delta}}\|_2 + \xi^2$. This is allowed since

$$\begin{aligned}|\tilde{\kappa}_\Sigma(\boldsymbol{\delta}_{\rm ref}) - \kappa_\Sigma(\boldsymbol{\delta}_{\rm ref})| &\leq 2\sqrt{L}\xi\|\boldsymbol{\delta}_{\rm ref}\|_2 + \xi^2, \quad (77)\\ &\leq 2\sqrt{L}\xi\|\hat{\boldsymbol{\delta}}\|_2 + \xi^2, \quad (78)\end{aligned}$$

by definition of $\boldsymbol{\delta}_{\rm ref}$.

With the above mapping of η and η', and the properties of κ_Σ in (67), we apply Theorem 2: if ρ is such that

$$\bar{\lambda}_{\max}\rho^2 \leq \tfrac{\tilde{U}\tilde{r}^2 - 2\sqrt{2}\xi}{\tilde{L}} = \tfrac{U\gamma_{\min}}{L\gamma_{\max}}(r^2 - \tfrac{2\sqrt{2}\xi}{U\gamma_{\min}}), \quad (79)$$

then (76) guarantees

$$\|\boldsymbol{\delta}_{\rm ref}\|_2^2 \leq \tfrac{\tilde{U}\tilde{r}^2 - 2\sqrt{2}\xi}{\tilde{L}} = \tfrac{U\gamma_{\min}}{L\gamma_{\max}}(r^2 - \tfrac{2\sqrt{2}\xi}{U\gamma_{\min}}), \quad (80)$$

and therefore Theorem 2 gives the bound $\|\hat{\boldsymbol{\delta}}\|_2^2 \leq \frac{\tilde{L}}{\tilde{U}}\,\bar{\lambda}_{\max}\rho^2 + \frac{4\sqrt{\tilde{L}}}{\tilde{U}}\,\xi\,\|\hat{\boldsymbol{\delta}}\|_2 + \frac{2}{\tilde{U}}\xi^2$. Finding the only positive root of the above order-2 polynomial in $\|\hat{\boldsymbol{\delta}}\|_2$ yields

$$\begin{aligned}\tilde{U}\,\|\hat{\boldsymbol{\delta}}\|_2 &\leq 2\sqrt{\tilde{L}}\xi + \sqrt{(4\tilde{L} + 2\tilde{U})\xi^2 + \tilde{L}\tilde{U}\bar{\lambda}_{\max}\rho^2}. \quad (81)\\ &\leq (4\sqrt{\tilde{L}} + \sqrt{2\tilde{U}})\xi + \sqrt{\tilde{L}\tilde{U}\bar{\lambda}_{\max}}\,\rho. \quad (82)\end{aligned}$$

Using the notation $R_{\rm P}$ defined in (32), we rewrite the above as

$$\|\hat{\boldsymbol{\delta}}\|_2 \leq \frac{4R_{\rm P} + \sqrt{2}}{\sqrt{\tilde{U}}}\xi + R_{\rm P}\bar{\lambda}_{\max}^{\frac{1}{2}}\rho. \quad (83)$$

Since $\bar{\lambda}_{\min}\|\hat{\boldsymbol{p}} - \boldsymbol{p}^*\|_2^2 \leq \|\hat{\boldsymbol{\delta}}\|_2^2$ by Lemma 4, we finally obtain (34) by using all the notations given in (32). Similarly, (80) is rewritten as (33) with those notations. This finally concludes the whole proof of Theorem 1.

D. Proof of Lemma 1

Proof. If $\mathcal{S}$ is differentiable and non-injective over $\mathcal{P}$, there exist two distinct parameters $\boldsymbol{p}_1, \boldsymbol{p}_2 \in \mathcal{P}$ such that $\mathcal{S}(\boldsymbol{p}_1) = \mathcal{S}(\boldsymbol{p}_2)$. From the mean value theorem, there is $\bar{\boldsymbol{p}} \in \mathcal{P}$ on the segment from $\boldsymbol{p}_1$ to $\boldsymbol{p}_2$ such that

$$0 = \mathcal{S}(\boldsymbol{p}_2) - \mathcal{S}(\boldsymbol{p}_1) = \boldsymbol{J}(\bar{\boldsymbol{p}})(\boldsymbol{p}_2 - \boldsymbol{p}_1), \quad (84)$$

meaning that $\lambda_{\min}\big(\boldsymbol{J}^\top(\bar{\boldsymbol{p}})\boldsymbol{J}(\bar{\boldsymbol{p}})\big) = 0 = \bar{\lambda}_{\min}$. □

REFERENCES

[1] H. Wang and P. Chu, "Voice source localization for automatic camera pointing system in videoconferencing," in *1997 IEEE International Conference on Acoustics, Speech, and Signal Processing*, vol. 1. Munich, Germany: IEEE Comput. Soc. Press, 1997, pp. 187–190.

[2] A. Marti, M. Cobos, and J. J. Lopez, "Real time speaker localization and detection system for camera steering in multiparticipant videoconferencing environments," in *2011 IEEE International Conference on Acoustics, Speech and Signal Processing (ICASSP)*. Prague, Czech Republic: IEEE, May 2011, pp. 2592–2595.

[3] S. Saponara and B. Neri, "Radar sensor signal acquisition and 3D FFT processing for smart mobility surveillance systems," in *2016 IEEE Sensors Applications Symposium (SAS)*. Catania, Italy: IEEE, Apr. 2016, pp. 1–6.

[4] C. Rascon and I. Meza, "Localization of sound sources in robotics: A review," *Robotics and Autonomous Systems*, vol. 96, pp. 184–210, Oct. 2017.

[5] A. Y. Majid, C. Van Der Horst, T. Van Rietbergen, D. JohannesZwart, and R. V. Prasad, "Lightweight Audio Source Localization for Swarm Robots," in *2021 IEEE 18th Annual Consumer Communications & Networking Conference (CCNC)*. Las Vegas, NV, USA: IEEE, Jan. 2021, pp. 1–6.

[6] S. Capobianco, L. Facheris, F. Cuccoli, and S. Marinai, "Vehicle Classification Based on Convolutional Networks Applied to FMCW Radar Signals," in *Traffic Mining Applied to Police Activities*, F. Leuzzi and S. Ferilli, Eds. Cham: Springer International Publishing, 2018, vol. 728, pp. 115–128, series Title: Advances in Intelligent Systems and Computing.

[7] M. Gottinger, M. Hoffmann, M. Christmann, M. Schutz, F. Kirsch, P. Gulden, and M. Vossiek, "Coherent Automotive Radar Networks: The Next Generation of Radar-Based Imaging and Mapping," *IEEE J. Microw.*, vol. 1, no. 1, pp. 149–163, Jan. 2021.

[8] E. Hanle, "Survey of bistatic and multistatic radar," *IEE Proc. F Commun. Radar Signal Process. UK*, vol. 133, no. 7, p. 587, 1986.

[9] A. Frischen, J. Hasch, and C. Waldschmidt, "A Cooperative MIMO Radar Network Using Highly Integrated FMCW Radar Sensors," *IEEE Trans. Microwave Theory Techn.*, vol. 65, no. 4, pp. 1355–1366, Apr. 2017.

[10] B. G. Stewart, A. Nesbitt, and L. Hall, "Triangulation and 3D location estimation of RFI and Partial Discharge sources within a 400kV substation," in *2009 IEEE Electrical Insulation Conference*. Montreal, QC, Canada: IEEE, May 2009, pp. 164–168.

[11] M. Szirtes and R. Cselko, "Comparative Examination of Iterative and Non- Iterative Algorithms for Partial Discharge Location Approximation in High Voltage Equipment," in *2019 16th Workshop on Positioning, Navigation and Communications (WPNC)*. Bremen, Germany: IEEE, Oct. 2019, pp. 1–6.

[12] J. Chen, J. Benesty, and Y. Huang, "Time Delay Estimation in Room Acoustic Environments: An Overview," *EURASIP J. Adv. Signal Process.*, vol. 2006, no. 1, p. 026503, Dec. 2006.

[13] J. Fresno, G. Robles, J. Martínez-Tarifa, and B. Stewart, "Survey on the Performance of Source Localization Algorithms," *Sensors*, vol. 17, no. 11, p. 2666, Nov. 2017.

[14] S. Kitić, C. Gaultier, and G. Pallone, "A Comparative Study of Multilateration Methods for Single-Source Localization in Distributed Audio," Jul. 2020, arXiv:1910.10661 [cs, eess].

[15] C. R. Berger and J. M. F. Moura, "Noncoherent compressive sensing with application to distributed radar," in *2011 45th Annual Conference on Information Sciences and Systems*. Baltimore, MD, USA: IEEE, Mar. 2011, pp. 1–6.

[16] S. Gogineni and A. Nehorai, "Target Estimation Using Sparse Modeling for Distributed MIMO Radar," *IEEE Trans. Signal Process.*, vol. 59, no. 11, pp. 5315–5325, Nov. 2011.

[17] G. Monnoyer, T. Feuillen, L. Jacques, and L. Vandendorpe, "Sparsity-Driven Moving Target Detection in Distributed Multistatic FMCW Radars," in *2019 IEEE 8th International Workshop on Computational Advances in Multi-Sensor Adaptive Processing (CAMSAP)*. Le gosier, Guadeloupe: IEEE, Dec. 2019, pp. 151–155.

[18] Z. Yu, J. Li, Q. Guo, and J. Ding, "Efficient Direct Target Localization for Distributed MIMO Radar With Expectation Propagation and Belief Propagation," *IEEE Trans. Signal Process.*, vol. 69, pp. 4055–4068, 2021.

[19] J. Bosse, O. Krasnov, and A. Yarovoy, "Direct target localization with an active radar network," *Signal Processing*, vol. 125, pp. 21–35, Aug. 2016.

[20] D. E. Hack, L. K. Patton, A. D. Kerrick, and M. A. Saville, "Direct Cartesian detection, localization, and de-ghosting for passive multistatic radar," in *2012 IEEE 7th Sensor Array and Multichannel Signal Processing Workshop (SAM)*. Hoboken, NJ, USA: IEEE, Jun. 2012, pp. 45–48.

[21] M. Cobos, A. Marti, and J. J. Lopez, "A Modified SRP-PHAT Functional for Robust Real-Time Sound Source Localization With Scalable Spatial Sampling," *IEEE Signal Process. Lett.*, vol. 18, no. 1, pp. 71–74, Jan. 2011.

[22] M. V. S. Lima, W. A. Martins, L. O. Nunes, L. W. P. Biscainho, T. N. Ferreira, M. V. M. Costa, and Bowon Lee, "A Volumetric SRP with Refinement Step for Sound Source Localization," *IEEE Signal Process. Lett.*, vol. 22, no. 8, pp. 1098–1102, Aug. 2015.

[23] R. Boora and S. K. Dhull, "Performance Evaluation of Iterative SRP-PHAT Techniques for Acoustic Source Localization," in *Proceedings of First International Conference on Computational Electronics for Wireless Communications*, S. Rawat, A. Kumar, P. Kumar, and J. Anguera, Eds. Singapore: Springer Nature Singapore, 2022, vol. 329, pp. 403–418, series Title: Lecture Notes in Networks and Systems.

[24] J. H. DiBiase, H. F. Silverman, and M. S. Brandstein, "Robust Localization in Reverberant Rooms," in *Microphone Arrays*, A. Lacroix, A. Venetsanopoulos, M. Brandstein, and D. Ward, Eds. Berlin, Heidelberg: Springer Berlin Heidelberg, 2001, pp. 157–180, series Title: Digital Signal Processing.

[25] P. Aarabi, "The Fusion of Distributed Microphone Arrays for Sound Localization," *EURASIP J. Adv. Signal Process.*, vol. 2003, no. 4, p. 860465, Mar. 2003.

[26] A. N. Bishop and P. N. Pathirana, "Localization of Emitters via the Intersection of Bearing Lines: A Ghost Elimination Approach," *IEEE Trans. Veh. Technol.*, vol. 56, no. 5, pp. 3106–3110, Sep. 2007.

[27] A. Alexandridis, G. Borboudakis, and A. Mouchtaris, "Addressing the data-association problem for multiple sound source localization using DOA estimates," in *2015 23rd European Signal Processing Conference (EUSIPCO)*, Aug. 2015, pp. 1551–1555, iSSN: 2076-1465.

[28] T. J. Wei and Y. H. Lun, "An empirical exploration of a simple deghosting method for multistatic radars," in *2015 IEEE Radar Conference (RadarCon)*, May 2015, pp. 1440–1445, iSSN: 2375-5318.

[29] A. Alexandridis and A. Mouchtaris, "Multiple Sound Source Location Estimation in Wireless Acoustic Sensor Networks Using DOA Estimates: The Data-Association Problem," *IEEE/ACM Transactions on Audio, Speech, and Language Processing*, vol. 26, no. 2, pp. 342–356, Feb. 2018, conference Name: IEEE/ACM Transactions on Audio, Speech, and Language Processing.

[30] A. A. Gorji, R. Tharmarasa, and T. Kirubarajan, "Widely Separated MIMO versus Multistatic Radars for Target Localization and Tracking," *IEEE Transactions on Aerospace and Electronic Systems*, vol. 49, no. 4, pp. 2179–2194, Oct. 2013, conference Name: IEEE Transactions on Aerospace and Electronic Systems.

[31] J. Liu, F. Lian, and M. Mallick, "Distributed compressed sensing based joint detection and tracking for multistatic radar system," *Information Sciences*, vol. 369, pp. 100–118, Nov. 2016.

[32] Y. C. Eldar, P. Kuppinger, and H. Bolcskei, "Block-Sparse Signals: Uncertainty Relations and Efficient Recovery," *IEEE Transactions on Signal Processing*, vol. 58, no. 6, pp. 3042–3054, Jun. 2010, conference Name: IEEE Transactions on Signal Processing.

[33] B. Li and A. P. Petropulu, "Distributed MIMO radar based on sparse sensing: Analysis and efficient implementation," *IEEE Transactions on Aerospace and Electronic Systems*, vol. 51, no. 4, pp. 3055–3070, Oct. 2015, conference Name: IEEE Transactions on Aerospace and Electronic Systems.

[34] J. P. Dmochowski, J. Benesty, and S. Affes, "A Generalized Steered Response Power Method for Computationally Viable Source Localization," *IEEE Transactions on Audio, Speech, and Language Processing*, vol. 15, no. 8, pp. 2510–2526, Nov. 2007, conference Name: IEEE Transactions on Audio, Speech, and Language Processing.

[35] M. Cobos, F. Antonacci, A. Alexandridis, A. Mouchtaris, and B. Lee, "A Survey of Sound Source Localization Methods in Wireless Acoustic Sensor Networks," *Wireless Communications and Mobile Computing*, vol. 2017, no. 1, p. 3956282, 2017, _eprint: https://onlinelibrary.wiley.com/doi/pdf/10.1155/2017/3956282.

[36] R. Boora and S. K. Dhull, "A TDOA-based multiple source localization using delay density maps," *Sādhanā*, vol. 45, no. 1, p. 204, Aug. 2020.

[37] H. Do, H. F. Silverman, and Y. Yu, "A Real-Time SRP-PHAT Source Location Implementation using Stochastic Region Contraction(SRC) on a Large-Aperture Microphone Array," in *2007 IEEE International Conference on Acoustics, Speech and Signal Processing - ICASSP '07*, vol. 1, Apr. 2007, pp. I–121–I–124, iSSN: 2379-190X.

[38] A. Marti, M. Cobos, J. J. Lopez, and J. Escolano, "A steered response power iterative method for high-accuracy acoustic source localization," *The Journal of the Acoustical Society of America*, vol. 134, no. 4, pp. 2627–2630, Oct. 2013.

[39] M. B. Çöteli, O. Olgun, and H. Hacıhabiboğlu, "Multiple Sound Source Localization With Steered Response Power Density and Hierarchical Grid Refinement," *IEEE/ACM Transactions on Audio, Speech, and Language Processing*, vol. 26, no. 11, pp. 2215–2229, Nov. 2018, conference Name: IEEE/ACM Transactions on Audio, Speech, and Language Processing.

[40] C. Knapp and G. Carter, "The generalized correlation method for estimation of time delay," *IEEE Transactions on Acoustics, Speech, and Signal Processing*, vol. 24, no. 4, pp. 320–327, Aug. 1976, conference Name: IEEE Transactions on Acoustics, Speech, and Signal Processing.

[41] T. Dietzen, E. De Sena, and T. van Waterschoot, "Low-Complexity Steered Response Power Mapping based on Nyquist-Shannon Sampling," in *2021 IEEE Workshop on Applications of Signal Processing to Audio and Acoustics (WASPAA)*, Oct. 2021, pp. 206–210, arXiv:2012.09499 [cs, eess].

[42] G. Monnoyer, T. Feuillen, M. Drouguet, L. Jacques, and L. Vandendorpe, "Grid Hopping: Accelerating Direct Estimation Algorithms for Multistatic FMCW Radar," Jul. 2023, arXiv:2307.16550 [eess].

[43] C. Ekanadham, D. Tranchina, and E. P. Simoncelli, "Recovery of Sparse Translation-Invariant Signals With Continuous Basis Pursuit," *IEEE Transactions on Signal Processing*, vol. 59, no. 10, pp. 4735–4744, Oct. 2011, conference Name: IEEE Transactions on Signal Processing.

[44] K. Fyhn, M. F. \. Duarte, and S. H. Jensen, "Compressive Parameter Estimation for Sparse Translation-Invariant Signals Using Polar Interpolation," *IEEE Transactions on Signal Processing*, vol. 63, no. 4, pp. 870–881, Feb. 2015, conference Name: IEEE Transactions on Signal Processing.

[45] K. C. Knudson, J. Yates, A. Huk, and J. W. Pillow, "Inferring sparse representations of continuous signals with continuous orthogonal matching pursuit," in *Advances in Neural Information Processing Systems*, vol. 27. Curran Associates, Inc., 2014.

[46] S. Mallat, "CHAPTER 1 - Sparse Representations," in *A Wavelet Tour of Signal Processing (Third Edition)*, S. Mallat, Ed. Boston: Academic Press, Jan. 2009, pp. 1–31.

[47] C. Elvira, R. Gribonval, C. Soussen, and C. Herzet, "When does OMP achieve exact recovery with continuous dictionaries?" *Applied and Computational Harmonic Analysis*, vol. 51, pp. 374–413, Mar. 2021.

[48] A. Hyvärinen and P. Hoyer, "Emergence of Phase- and Shift-Invariant Features by Decomposition of Natural Images into Independent Feature Subspaces," *Neural Computation*, vol. 12, no. 7, pp. 1705–1720, Jul. 2000.

[49] R. Grosse, R. Raina, H. Kwong, and A. Y. Ng, "Shift-Invariance Sparse Coding for Audio Classification," Jun. 2012, arXiv:1206.5241 [cs, stat].

[50] R. Gribonval, "Fast matching pursuit with a multiscale dictionary of Gaussian chirps," *IEEE Transactions on Signal Processing*, vol. 49, no. 5, pp. 994–1001, May 2001, conference Name: IEEE Transactions on Signal Processing.

[51] L. Jacques and C. De Vleeschouwer, "A Geometrical Study of Matching Pursuit Parametrization," *IEEE Transactions on Signal Processing*, vol. 56, no. 7, pp. 2835–2848, Jul. 2008, conference Name: IEEE Transactions on Signal Processing.

[52] Y. Traonmilin and J.-F. Aujol, "The basins of attraction of the global minimizers of the non-convex sparse spike estimation problem," Sep. 2019, arXiv:1811.12000 [cs, math].

[53] F. Champagnat and C. Herzet, "Atom Selection in Continuous Dictionaries: Reconciling Polar and SVD Approximations," in *ICASSP 2019 - 2019 IEEE International Conference on Acoustics, Speech and Signal Processing (ICASSP)*, May 2019, pp. 5516–5520, iSSN: 2379-190X.

[54] R. Niu, R. S. Blum, P. K. Varshney, and A. L. Drozd, "Target Localization and Tracking in Noncoherent Multiple-Input Multiple-Output

Radar Systems," *IEEE Trans. Aerosp. Electron. Syst.*, vol. 48, no. 2, pp. 1466–1489, Apr. 2012.
[55] L. Han, X. Liu, N. Zhang, S. Wu, J. Zhu, and Z. Xu, "Two-dimensional multi-snapshot newtonized orthogonal matching pursuit for doa estimation," *Digital Signal Processing*, vol. 121, p. 103313, 2022.
[56] R. Baraniuk and P. Steeghs, "Compressive Radar Imaging," in *2007 IEEE Radar Conference*, Apr. 2007, pp. 128–133, iSSN: 2375-5318.
[57] B. Han, "The Research of Velocity Compensation Method Based on Range-Profile Function," *IJHIT*, vol. 7, no. 2, pp. 49–56, Mar. 2014.
[58] T. Feuillen, A. Mallat, and L. Vandendorpe, "Stepped frequency radar for automotive application: Range-Doppler coupling and distortions analysis," in *MILCOM 2016 - 2016 IEEE Military Communications Conference*, Nov. 2016, pp. 894–899, iSSN: 2155-7586.
[59] G. Wang, J.-M. Muñoz-Ferreras, C. Gu, C. Li, and R. Gómez-García, "Application of Linear-Frequency-Modulated Continuous-Wave (LFMCW) Radars for Tracking of Vital Signs," *IEEE Transactions on Microwave Theory and Techniques*, vol. 62, no. 6, pp. 1387–1399, Jun. 2014, conference Name: IEEE Transactions on Microwave Theory and Techniques.
[60] G. Monnoyer, T. Feuillen, L. Vandendorpe, and L. Jacques, "Sparse Factorization-Based Detection of Off-the-Grid Moving Targets Using FMCW Radars," in *ICASSP 2021 - 2021 IEEE International Conference on Acoustics, Speech and Signal Processing (ICASSP)*, Jun. 2021, pp. 4575–4579, iSSN: 2379-190X.
[61] J. Aleksandravicius, N. Decarli, A. Guerra, and D. Dardari, "High-accuracy localization of backscattering uwb tags: Implementation and experimental results," in *2017 IEEE International Conference on RFID Technology & Application (RFID-TA)*, Sep. 2017, pp. 34–39.
[62] L. Wang, Y. Yang, and X. Liu, "A Direct Position Determination Approach for Underwater Acoustic Sensor Networks," *IEEE Transactions on Vehicular Technology*, vol. 69, no. 11, pp. 13 033–13 044, Nov. 2020, conference Name: IEEE Transactions on Vehicular Technology.
[63] D. Pavlidi, A. Griffin, M. Puigt, and A. Mouchtaris, "Real-Time Multiple Sound Source Localization and Counting Using a Circular Microphone Array," *IEEE Transactions on Audio, Speech, and Language Processing*, vol. 21, no. 10, pp. 2193–2206, Oct. 2013, conference Name: IEEE Transactions on Audio, Speech, and Language Processing.
[64] A. Weiss, "Direct position determination of narrowband radio frequency transmitters," *IEEE Signal Processing Letters*, vol. 11, no. 5, pp. 513–516, May 2004, conference Name: IEEE Signal Processing Letters.
[65] B. Demissie, M. Oispuu, and E. Ruthotto, "Localization of multiple sources with a moving array using subspace data fusion," in *2008 11th International Conference on Information Fusion*, Jun. 2008, pp. 1–7.
[66] G. Chardon, "Theoretical analysis of beamforming steering vector formulations for acoustic source localization," *Journal of Sound and Vibration*, vol. 517, p. 116544, Jan. 2022.
[67] J. Zhu, L. Han, R. S. Blum, and Z. Xu, "On the analysis of the fisher information of a perturbed linear model after random compression," *IEEE Signal Processing Letters*, vol. 25, no. 1, pp. 100–104, 2018.
[68] H. Godrich, A. M. Haimovich, and R. S. Blum, "Target localization accuracy gain in mimo radar-based systems," *IEEE Transactions on Information Theory*, vol. 56, no. 6, pp. 2783–2803, 2010.
[69] A. G. Amigó, P. Closas, A. Mallat, and L. Vandendorpe, "Cramér-rao bound analysis of uwb based localization approaches," in *2014 IEEE International Conference on Ultra-WideBand (ICUWB)*, 2014, pp. 13–18.